https://doi.org/10.5194/egusphere-2025-3481
Preprint. Discussion started: 20 August 2025

Aerosol variability over oceans using micro-pulse lidar and photometer: Insights from TRANSAMA ship-based campaign

Maria Fernanda Sanchez-Barrero[1], Philippe Goloub[1], Luc Blarel[1], Ioana Elisabeta Popovici[1,2], Benjamin Torres[1], Gaël Dubois[1], Thierry Podvin[1], Fabrice Ducos[1], Romain de Filippi[1], Michaël Sicard[3,4], Viviane Bout Roumazeilles[5], Charlotte Skonieczny[6]

[1]Univ. Lille, CNRS, UMR 8518 - LOA - Laboratoire d'Optique Atmosphérique, F-59000 Lille, France
[2]R&D Department, CIMEL Electronique, 75011 Paris, France
[3]Univ. La Réunion, CNRS, UMR 8105 - LACy - Laboratoire de l'Atmosphère et des Cyclones, Météo-France, 97400 Saint-Denis de La Réunion, France
[4]CommSensLab-UPC, Universitat Politècnica de Catalunya, Barcelona, 08034, Spain
[5]Univ. Lille, CNRS-UMR8217, Laboratoire Géosystèmes, 59655 Lille, France
[6]Univ. Paris-Saclay, CNRS, UMR 8148 - GEOPS - Laboratoire Géosciences Paris-Saclay, 91405 Orsay Cedex, France

Correspondence to: Maria F. Sanchez-Barrero (mariafernanda.sanchezbarrero@univ-lille.fr)

Abstract. The TRANSAMA campaign (Transit to AMARYLLIS-AMAGAS oceanographic cruise), conducted aboard the research vessel *Marion Dufresne II* investigated aerosol properties during its transit from La Reunion Island to Barbados (April–May 2023). A set of remote sensing instruments, including two CE318-T Sun-sky-lunar photometers and a CE370 single-wavelength elastic lidar, was deployed under the MAP-IO (Marion Dufresne Atmospheric Program–Indian Ocean) framework. Synergistic observations provided vertically resolved aerosol properties, such as extinction coefficients, alongside atmospheric structure, highlighting the marine boundary layer (MBL) top at 800 ± 300 m. While the photometer observations revealed very clean atmospheric conditions over the South Atlantic ($AOD(440) = 0.08 \pm 0.04$), thin aerosol layers above the MBL were identified as long-range transported residual biomass-burning-urban aerosols from Southern Africa with effective LR of 33 ± 12 sr. Cloud layers covering a large range of altitudes (up to 16 km) were observed in 53% of the lidar profiles with higher occurrence in low altitudes where the aerosol content was higher. These findings emphasize the impact of continental aerosols on remote oceanic regions, with implications on cloud formation and climate processes. The campaign also facilitated performance assessments of the deployed instrumentation, supporting the development of advanced mobile observatories for coupled lidar-photometer systems in marine environments.

https://doi.org/10.5194/egusphere-2025-3481
Preprint. Discussion started: 20 August 2025

1 Introduction

Aerosols play a critical role in atmospheric processes, influencing climate, air quality and human health. Despite substantial advancements in aerosol research, significant uncertainties remain associated to aerosol radiative impacts (Boucher et al., 2013; Szopa et al., 2021). Marine aerosols, primarily sea spray consisting of sea salt and organic matter, dominate aerosol content over the oceans, which cover more than 70% of the Earth's surface. Wind speed is the primary factor driving the generation of natural marine aerosols (Smirnov et al., 2012; Sun et al., 2024). These aerosols mainly exhibit high scattering efficiency and hygroscopicity enforcing cloud formation (Pierce and Adams, 2006; Jaeglé et al., 2011; Burton et al., 2013; Bohlmann et al., 2018). Their interaction with continental aerosols, such as Saharan dust transported over the Atlantic (Kanitz et al., 2014; Bohlmann et al., 2018; Barreto et al., 2022), or biomass burning aerosols in the Southern hemisphere (Duflot et al., 2011; Chazette et al., 2019; Formenti et al., 2019; Ranaivombola et al., 2025), are critical for understanding climate feedbacks.

Observations from satellite and ground-based platforms over remote islands have shown that aerosol optical depth (AOD) in pristine oceanic regions, such as the South Atlantic, South Indian, and Pacific Oceans, is typically lower than 0.1, providing insights into pre-industrial conditions and aerosol-climate interactions (Koren et al., 2014; Mallet et al., 2018; Duflot et al., 2022). Small changes in such low aerosol loadings can significantly impact cloud formation, as suggested by Koren et al. (2014). However, discrepancies between satellite-derived AOD and ground-based measurements highlight the need of enhanced aerosol ground-based observations over oceans (Mallet et al., 2018; Ranaivombola et al., 2023 and references therein).

Ship-based observatories offer a unique opportunity to fill observational gaps in remote oceanic regions. Sun photometer maritime observations were deployed by the Maritime Aerosol Network (MAN; Smirnov et al., 2009), an initiative of the world-wide open-access photometer network AERONET (AErosol Robotic NETwork; Holben et al., 1998). MAN collects AOD at five wavelengths manually with Microtops II handheld Sun photometers onboard ship cruises (Duflot et al., 2011; Smirnov et al., 2012). Though, these measurements are limited to the availability of observers and the instrument precision. In recent years, the multispectral Sun-sky-lunar CIMEL CE318-T photometer (Barreto et al., 2016), widely used and designed by the French company Cimel, has been fully adapted for automatic observations onboard ships (Yin et al., 2019). Likewise, the PLASMA (Photomètre Léger Aéroporté pour la Surveillance des Masses d´Air; Karol et al., 2013) sun-photometer, developed and deployed by the Laboratoire d'Optique Atmospherique (LOA, Lille University) exclusively for mobile measurements, has performed measurements aboard aircraft and vehicles during field campaigns (Mascaut et al., 2022; Popovici et al., 2018, 2022; Sanchez Barrero et al., 2024). Both CE318-T and PLASMA photometers are fully adapted to AERONET data processing.

https://doi.org/10.5194/egusphere-2025-3481
Preprint. Discussion started: 20 August 2025

Studies conducted with lidars aboard mobile vectors (car, aircraft and ship) during field campaigns showed the possibility to support satellite-based observations (Burton et al., 2013; Warneke et al., 2023), assess air quality in urban- rural transitions and complex topographies (Royer et al., 2011; Chazette et al., 2012; Chazette and Totems, 2023; Dieudonné et al., 2015; Popovici et al., 2018, 2022; Shang et al., 2018; Sanchez Barrero et al., 2024) and characterize transported aerosols over oceans (Duflot et al., 2011; Burton et al., 2013; Kanitz et al., 2014; Yin et al., 2019). However, installing specialized lidars for unattended observations, such as multi-wavelength Raman or HSRL (High Spectral Resolution Lidar) systems, onboard mobile vector remains challenging due to their high dependence on environmental conditions and opto-mechanical stability. Thus, the use of compact automatic micropulse lidar systems is proposed for continuous mobile observations. The main limitation of such a system is given by the assumptions needed to derive aerosol properties, which can be overcome by coupling the vertical resolved lidar and column-integrated photometer observations. For instance, a description of a compact and light mobile system, integrating a compact lidar and a sun photometer was first presented by Popovici et al. (2018). This unique system, deployed by LOA, included the CE370 single-wavelength elastic lidar, deployed by CIMEL company, and the PLASMA sun-photometer. During several field campaigns the integrated system performed on-road mobile measurements (Popovici et al., 2018, 2022; Warneke et al., 2023; Sanchez Barrero et al., 2024), demonstrating its versatility for aerosol characterization.

The MAP-IO platform (http://www.mapio.re/, last access: December 6, 2024) is a French National Instrumental facility aboard the *Marion Dufresne II* research vessel (RV), the largest oceanographic ship of the French fleet operated by the IFREMER (Institut Français de Recherche pour l'Exploitation de la Mer, https://www.ifremer.fr/, last access: December 6 2024). The MAP-IO program, part of ACTRIS-ERIC, aims to study ocean-atmosphere processes in a long-term basis to assess climate studies (Tulet et al., 2024). The observatory integrates a radiometer (measuring solar flux), in-situ instruments for gas and aerosol monitoring and a ship-adapted CE318-T photometer, all of them measuring since 2021. The successful experience of the first three years of photometer measurements aboard *Marion Dufresne II* leaded to the installation of ship-adapted CE318-T photometers on other research vessels (Torres et al., 2025), underlining the growing recognition of the need for comprehensive marine aerosol monitoring.

The oceanographic cruise AMARYLLIS-AMAGAS, conducted aboard the *Marion Dufresne II* RV, took place from 16 May to 3 July 2023 (Govin et al., 2024). The Franco-Brazilian campaign essentially aimed to study the Amazon's role in past climates using core sediments. TRANSAMA (Transit to AMARYLLIS-AMAGAS) campaign emerged as initiative to valorize the transit (April-May 2023) from Le Port, La Reunion Island (*Marion Dufresne II* main port; 20.94 °S, 55.29 °E) to Bridgetown, Barbados (mission's starting port, 13.10 °N, 59.63 °W). TRANSAMA employed a combination of remote sensing instruments, including the installation of a second CE318-T photometer and the CE370 elastic lidar, to investigate the aerosol properties along the ship's route covering the South Indian and the Atlantic oceans. The field campaign also provided the opportunity to perform operational assessments on the instrumentation embarked.

https://doi.org/10.5194/egusphere-2025-3481
Preprint. Discussion started: 20 August 2025

The primary objective of this study is to enhance our understanding of aerosol properties in marine environments through the synergistic application of micropulse lidar and ship-adapted photometers during the TRANSAMA campaign (April–May 2023). This work focuses on characterizing the vertical distribution of aerosols and clouds across the South Indian and Atlantic Oceans, with particular attention to the influence of long-range transported continental aerosol plumes on remote oceanic regions. The study also aims to validate and assess the performance of an integrated lidar-photometer system under challenging conditions, demonstrating its capability (and limitations) for continuous and autonomous observations. By bridging observational gaps over oceans, this approach contributes to ongoing discussions on aerosol-climate interactions, satellite calibration and validation, and emphasizes the need for comprehensive observational strategies in marine environments.

This work presents the description and setup of the remote sensing instrumentation used during the TRANSAMA campaign in Section 2. The data processing and quality control for both lidar and photometer are presented in Section 3. Results and discussion of the observed aerosol properties in maritime environment are presented in Section 4, highlighting atmospheric structure and transatlantic transport.

2 Remote sensing instrumentation

This section outlines the mobile remote sensing instruments used in this study. Subsection 2.1 describes the CE370 lidar, while subsection 2.2 describes the CE318-T photometer. The instrumentation setup during the TRANSAMA campaign is detailed in Subsection 2.3.

2.1 Single-wavelength lidar

The ***CE370 lidar*** is an eye-safe, single-wavelength micro-pulse elastic lidar operating at 532 nm with a 20 μJ pulse energy at a 4.7 kHz repetition rate. Designed by Cimel Electronique, it utilizes a shared transmitter/receiver telescope (diameter of 20 cm and half field of view of 55 μrad) connected via an 10 m optical fiber to its laser source and control system (laser divergence of 240 $mrad$). Photon-counting with an avalanche photodiode (APD) detects the elastic backscattered signals, enabling monitoring of aerosol and cloud properties in the troposphere with a vertical resolution of 15 m and one minute accumulation time (Pelon et al., 2008; Mortier et al., 2013; Popovici et al., 2018).

For field campaigns, the CE370 lidar coupled with a photometer has been deployed on ground-based mobile platforms. The system has demonstrated its capability to characterize vertical aerosol properties under diverse conditions, including highly polluted urban areas, proximity to fire sources, and rugged terrain during platform movement (Popovici et al., 2018, 2022; Hu et al., 2019; Sanchez Barrero et al., 2024).

https://doi.org/10.5194/egusphere-2025-3481
Preprint. Discussion started: 20 August 2025

2.2. Photometers

The CIMEL ***CE318-T Sun-sky-lunar photometer*** (Barreto et al., 2016) performs automated direct sun and lunar measurements across nine spectral channels (340–1640 nm). It measures aerosol optical depth (AOD, accuracy ± 0.01) and extinction Angstrom exponent (EAE), while multi-angular sky radiance measurements enable retrievals of aerosol microphysical properties, such as volume size distribution, refractive index, and single-scattering albedo (Dubovik and King, 2000; Sinyuk et al., 2020). For ship-borne applications, the CE318-T is equipped with GPS and compass modules to correct for ship's attitude (heading, pitch and roll), ensuring accurate Sun and Moon tracking (Yin et al., 2019). Since January 2021, it has been operational aboard the *Marion Dufresne II* RV as part of the MAP-IO project (Tulet et al., 2024) which successful three years of continuous measurements were presented by Torres et al. (2025).

2.3 Instrumentation setup

The CE318-T ship-borne photometer (# 1273) operational since 2021 aboard the *Marion Dufresne II*, *photometer A* hereafter, was installed on the ship's main mast (Fig. 1) to minimize potential obstacles on tracking. Its continuous observations revealed technical challenges, such as wrong Sun-Moon tracking due to strong waves combining with a rather slow communication between the control/acquisition software and GPS-compass module. To address these challenges, a second CE318-T photometer installed during TRANSAMA was used for test and validation (see Section 3.2). The second photometer (# 1243), *photometer B* hereafter, was installed on deck I (Fig. 1) and accounted for an updated software to improve the tracking response. In addition, PLASMA-3 photometer was installed on deck I, next to photometer B, for a first assessment of its lunar measurements nevertheless results remain preliminary and are not included in this work.

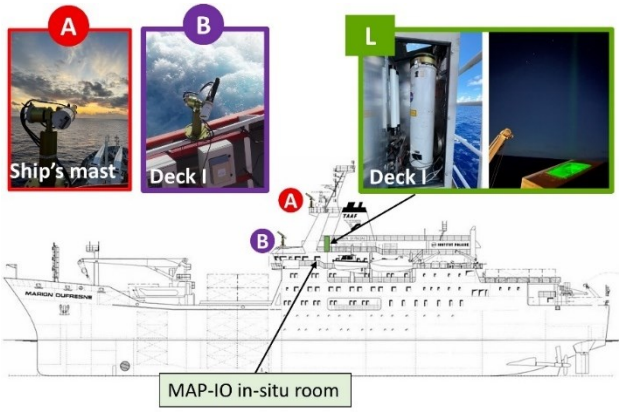

Figure 1. Distribution of the remote sensing instrumentation aboard *Marion Dufresne* RV during the TRANSAMA campaign. The location of the two CE318-T photometers (A and B) and the CE370 single-wavelength lidar (L) are indicated.

The CE370 single-wavelength lidar was also deployed during the campaign. Its laser source was housed in the temperature-controlled MAP-IO in-situ room, featuring vibration isolation and movement dissipation structure. The transmission/reception

https://doi.org/10.5194/egusphere-2025-3481
Preprint. Discussion started: 20 August 2025

telescope was installed on Deck I within an enclosure equipped with an automatic blind system to prevent direct sunlight exposure and regulated temperature to avoid condensation on the window (Fig. 1). However, the constant sea spray produced by the waves hitting the vessel deposited and dried on top of the lidar window resulting in the attenuation of the laser beam. A frequent cleaning was reinforced to avoid the laser attenuation.

All remote sensing instruments transmitted acquired raw data to the LOA server (PHOTONS, University of Lille), the photometers every 15 minutes and lidar every hour, for data-processing and visualization. Photometer data is then forwarded to the NASA server to undergo AERONET data treatment (Section 3.2). The protocol for data acquisition of the ship-adapted photometer is thoroughly described by Torres et al. (2025) along with the extended description of the system.

In the framework of MAP-IO project, ancillary data is provided from a Vaisala weather transmitter (WXT530) installed in the main mast. It provides meteorological measurements every 5 seconds, including temperature (accuracy: $\pm 0.3\ °C$), pressure (accuracy: $\pm 0.5\ hPa$ at 0-30 $°C$), relative humidity (accuracy: ± 3 %), wind speed (rel. accuracy: ± 3 % at 10 m/s) and wind direction (accuracy: ± 3 ° at 10 m/s). The wind measurements reflect the apparent wind speed and direction. To obtain the true wind speed and direction, vectorial addition is employed, using the vessel's heading and speed to accurately account for the motion of the ship.

3 Data processing and quality control

This section focuses on the methodology employed to study aerosol properties and the atmospheric structure passing through the rigor of quality assurance procedures. The lidar data processing is presented in Section 3.1, including the description of quality control procedure (Sect. 3.1.1), detection limits (Sect. 3.1.2) and detection of MBL top, aerosol and cloud layers (Sect. 3.1.3). The photometer data quality control is presented in Section 3.2, including a multi-factor analysis of the ship-adapted photometer detection limits (Sect. 3.2.1). The inversion methods used to derive aerosol properties combining lidar and photometer are presented in Section 3.3.

3.1 Lidar data processing

The detected backscattered lidar signal is represented by equation (1) (Kovalev and Eichinger, 2004), with the wavelength dependency omitted for simplicity:

$$RCS(r) = C_L[\beta_{mol}(r)+\beta_{aer}(r)]exp\,(-2\int_0^r \alpha_{mol}(r')dr')\,exp\,(-2\int_0^r \alpha_{aer}(r')dr') \quad (1)$$

$$\beta_{att}(r) = \frac{RCS(r)}{C_L} \quad (2)$$

https://doi.org/10.5194/egusphere-2025-3481
Preprint. Discussion started: 20 August 2025

The right side of Eq. (1) describes the range-corrected signal (RCS, in photons s^{-1} m^2) in terms of the atmospheric optical properties, calibrated using the constant C_L (in photons s^{-1} m^3 sr). The backscatter coefficient $\beta(r)$ (or BSC in $m^{-1}sr^{-1}$) and the extinction coefficient $\alpha(r)$ (or EXT in m^{-1}) are distinguished by subscripts for molecular (mol) and aerosol (aer) contributions. Thus, the total attenuated backscatter $\beta_{att}(r)$ (in $m^{-1}sr^{-1}$) defined in Eq. (2) accounts for both contributions.

Key instrumental corrections—including background subtraction (B), after-pulse and dead time effects, overlap function (O), and range dependence (r^2)—are applied to derive the RCS, following established methods (Pelon et al., 2008; Mortier et al., 2013; Popovici et al., 2018).

3.1.1 Data quality control and normalization

Quality control of lidar data involves the Rayleigh fit procedure (Freudenthaler et al., 2018), that is, normalizing RCS(r) to a modeled molecular profile $\beta_{mol}(r)\exp\left(-2\int_0^r \alpha_{mol}(r)\,dr'\right)$ in a reference zone (r_{ref}) assumed to be free of aerosols ($\beta_{aer}(r_{ref}) = 0$). Molecular backscatter and extinction coefficients are calculated using temperature and pressure profiles from standard models or radiosonde data. The slope index, defined as the ratio of normalized RCS to molecular profile slopes in the reference zone, evaluates lidar performance (a slope index closes to 1 indicates good performance). When photometer AOD data is available and clean conditions are met, the lidar calibration is determined (C_L) (Sanchez-Barrero et al., 2024 and references therein).

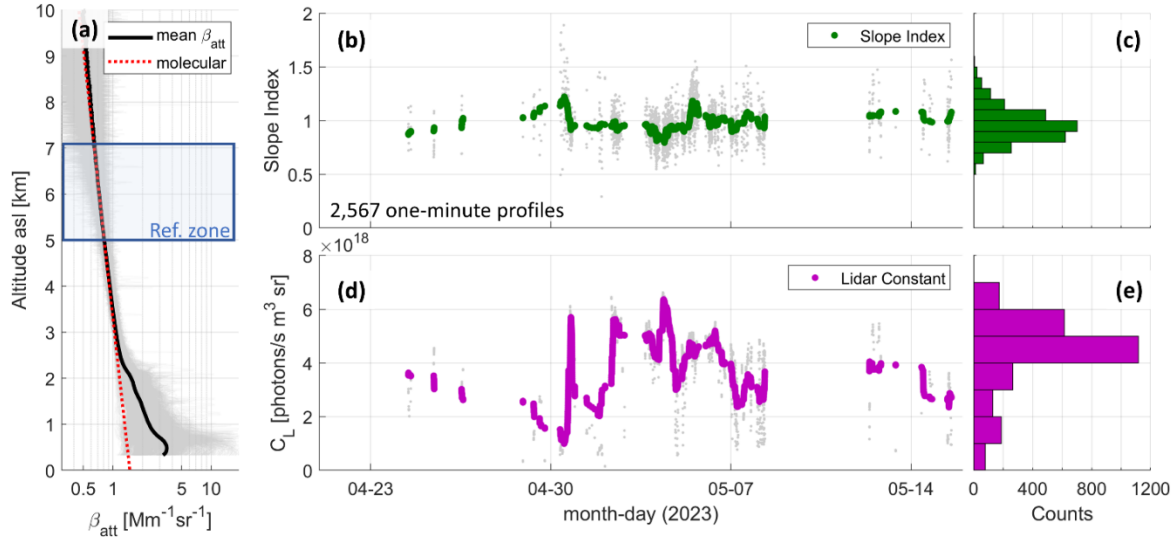

Figure 2. Data quality control of lidar profiles. (a) Rayleigh fit procedure was applied on 2,567 profiles (10 % of total) when clean conditions were met and AOD from photometer was available. The slope index temporal series (b) and histogram (c) are presented, along with the derived lidar constant (C_L) temporal series (d) and histogram (e). The AOD data used for the lidar constant calculation correspond to level 1.5 data of photometer B (#1243).

https://doi.org/10.5194/egusphere-2025-3481
Preprint. Discussion started: 20 August 2025

Figure 2 resumes the lidar data quality control performed for TRANSAMA data. From a total of 26,215 one-minute profiles generated during the campaign, a set of 2,567 Rayleigh fits (Fig. 2(a)) have been performed when clean conditions were met, i.e., no clouds and AOD at 532 nm below 0.1. Coincident photometer measurements are accounted within a 5-minute threshold. The reference zone r_{ref} was defined between 5 and 7 km a.s.l. (above sea level), and the molecular coefficients were calculated using the tropical standard atmosphere. From the Rayleigh fits performed, slope indexes (Fig. 2b and 2c) and the lidar calibration constant (Fig. 2d and 2e) were calculated. This analysis confirmed the good performance of the lidar system during the campaign, with a slope index showing an overall low bias of 4% relative to the molecular attenuated backscatter profile and a 16% error margin despite the considerable noise induced by solar irradiance. However, frequent laser attenuation due to sea spray deposition on the lidar window prevented a consistent lidar constant for the dataset, with values varying a 30 % relative to the mean ($C_L = (4.3 \pm 1.4) \times 10^{18}\ photons/s\,m^3 sr$).

Therefore, a normalized relative backscatter (NRB) was defined instead (Lopatin et al., 2013).

$$NRB(r) = \frac{RCS(r)}{\int_{r_o}^{r_{max}} RCS(r\prime)dr\prime} \quad (3)$$

Where r_o is the lower detection limit (Sect. 3.1.2), and r_{max} is set at 10 km consistent with prior studies (Welton and Campbell, 2002; Lopatin et al., 2013, 2024). In particular the NRB profiles improve studies on atmospheric structure and data visualization, but do not have an impact on the later inversion procedure (Section 3.3) while the detection limits are not strongly affected.

3.1.2 Detection limits

The detection limits of the CE370 lidar primarily depend on signal-to-noise ratio (SNR) and the overlap function as discussed in previous studies (Popovici et al., 2018; Sanchez Barrero et al., 2024). The lower detection limit (blind zone) was defined at 350 m, where overlap function uncertainties exceed 20 %. The upper detection limit, determined by SNR < 1.5, varies between 10 and 18 km due to background noise from solar irradiance and the laser beam attenuation.

Significant motion of the RV caused by rough seas, resulting in high variation in pitch or roll, introduces negligible uncertainties in the lidar profiling. For example, a 5-degree tilt in any direction causes altitude errors of 0.3% and horizontal shifts of 0.1% relative to the zenith. Furthermore, the system's combination of a wide laser divergence and a narrow telescope field of view minimizes misalignments due to platform motion. Additionally, the lidar's slightly offset viewing angle reduces direct reflections from clouds, enhancing measurement quality.

Once the lidar detection limits have been defined and the NRB profiles obtained, the following subsection outlines the methodology implemented to determine the atmospheric structure from each lidar profile measured.

https://doi.org/10.5194/egusphere-2025-3481
Preprint. Discussion started: 20 August 2025

3.1.3 Atmospheric structure detection

Atmospheric structure detection is applied individually to each one-minute lidar profile to capture transient cloud events. The methodology follows BASIC algorithm (Mortier, 2013), developed by the LOA, and STRAT (Morille et al., 2007), a dedicated software for atmospheric structure detection. Molecular regions are identified using STRAT, while aerosol and cloud layers are detected via the gradient method in BASIC. The layer base and peak are determined by the first derivative of the NRB signal with threshold to exclude wrong detection. An initial filtering using the threshold (T1) is defined as $NRB(r_{peak}) - NRB(r_{base}) > T1 \times N(r_{base})$, where N is the noise level. The distinction between aerosol and cloud layers is determined using a second threshold (T2), where the ratio $NRB(r_{peak})/\ NRB(r_{base})\ > T2$ indicates the presence of a cloud layer.

The marine boundary layer (MBL) top is detected using the Haar wavelet covariance transform (WCT) method (Flamant et al., 1997; Brooks, 2003; Baars et al., 2008; Granados-Muñoz et al., 2012). The maximum in the WCT profile in the range 0.35-3 km identifies the MBL top. Clouds often form at the top of the boundary layer (Stull, 1988; Bechtold and Siebesma, 1998; Kotthaus et al., 2023); thus, in cases where low clouds are detected, the MBL detection is constrained to the cloud base.

For this study, the threshold T1 was set to 5 and T2 was set to 4, based on guidance from previous works (Morille et al., 2007; Mortier, 2013; Mortier et al., 2016). If the upper detection limit of the profile, falls within the blind zone (below 350 m), the profile is considered saturated, which could result from condensation, fog or very low-level clouds.

Having defined the methods used for lidar data processing, the following section introduces the photometer data processing.

3.2 Photometer data processing

The ship-adapted CE318-T photometer employs AERONET's data processing protocols to enable near real-time (NRT) aerosol monitoring with rigorous quality screening (Smirnov et al., 2000; Holben et al., 2006; Giles et al., 2019). These protocols, consistent with those applied to fixed land-based AERONET sites, are implemented using Version 3 algorithms (Giles et al., 2019).

The instrument performs the so-called Sun-Moon triplet measurements, meaning that a sequence of measurements at all wavelengths is taken three times separated by thirty seconds resulting in one-minute averaged measurement (data level 0 or L0). Data is primarily classified as level 1 (or L1), when the root-mean-square error (RMSE) of the triplet measurements relative to one-minute averaged is below 16 % (Eck et al., 2014). L1 data undergoes further cloud screening to qualify as Level 1.5 (L1.5). Multiple quality control procedures are then applied, including the AOD triplet variability criteria, Angstrom exponent limitations, AOD stability and smoothness checks (Giles et al., 2019). Data at level 2 and downward sky radiance inversions are not yet routinely available for in-motion measurements (Torres et al., 2025). Dense aerosol layers, thin cirrus clouds (AOD < 0.03), and obstacles can introduce uncertainties on the measurements (Eck et al., 2014; Giles et al., 2019).

https://doi.org/10.5194/egusphere-2025-3481
Preprint. Discussion started: 20 August 2025

3.2.1 Data quality control and instrument performance

A multifactor analysis was conducted to evaluate the ship-adapted photometer performances. This analysis correlated the proportion of measurements passing L1 and L1.5 screenings with main influencing factors. Conditional counts, i.e., counts of values meeting specific thresholds, were used to intercompare parameters, including:

- *Apparent wind speed (WS):* Measured by the main mast weather station.
- *Vessel attitude variability (HPRe)*: quantified by the combined RMSE of heading, pitch, and roll (Eq. 4).

$$HPRe = \sqrt{RMSE_{heading}^2 + RMSE_{pitch}^2 + RMSE_{roll}^2} \quad (4)$$

- *Cloud coverage:* Derived from lidar measurements and categorized as no clouds, low-to-mid clouds ($\leq 7\ km$), and high-altitude clouds ($> 7\ km$).
- *Photometer measurements:* RMSE of the triplet measurement (Ve) for L0 to L1, and zenith angle (ZA) for L1 to L1.5 analysis. Zenith angles were categorized as low (ZA < 30°), mid (30° < ZA < 60°) and high (ZA > 60°).

Thresholds for WS and HPRe were determined using 25th, 50th and 75th percentiles. Photometer data points were matched with corresponding variables within a 30-second window, consistent with the triplet duration. Data lacking one or more associated metrics were excluded from the analysis.

Results of the multifactor analysis for both A and B photometers are presented in Figures 3 and 4. Histograms (Figs. 3a, 3b, 4a and 4b) show the total number of measurements captured at each threshold (at L0 in Fig. 3 and L1 in Fig. 4), while heatmaps (Figs. 3c, 3d, 4c and 4d) display relative conditional counts (upper right side) of the parameters and the frequency of measurements passing the screenings (lower left side).

Figure 3 illustrates the L0 to L1 screening process, comprising 3,786 triplet measurements (L0) for photometer A and 4,099 for photometer B. This corresponds to 85% and 86% of total measurements, respectively, comprising Sun and Moon observations. Of these, 50% (A) and 55% (B) met the triplet variance criterion (Ve≤16%). However, the 37% (A) and 40% (B) of observations qualified as L1, due to additional requirements, such as minimum daily observations, optical air mass range, and radiometer sensitivity (Giles et al., 2019). Measurements failing L1 triplet variance protocol (40% A, 45% B) were largely associated with low-to-mid cloud occurrence and/or higher vessel instability $HPRe > 1.3°$, reflecting the impact of ship motion on Sun-Moon tracking.

https://doi.org/10.5194/egusphere-2025-3481
Preprint. Discussion started: 20 August 2025

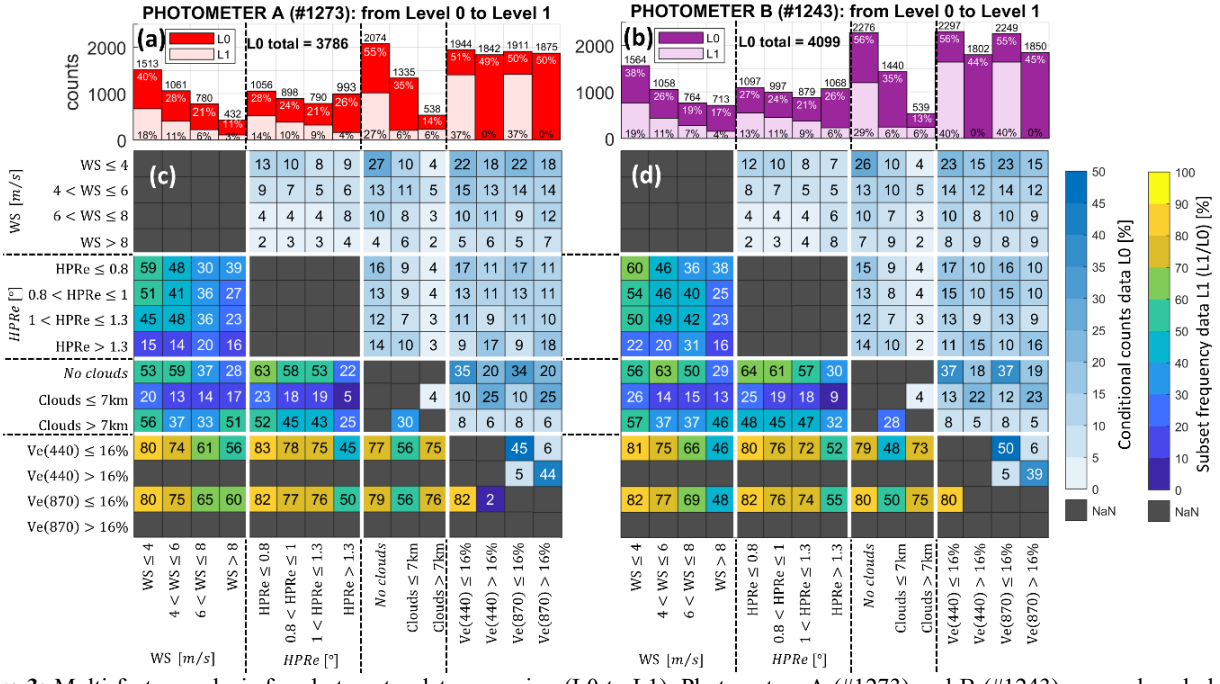

Figure 3: Multi-factor analysis for photometer data screening (L0 to L1). Photometers A (#1273) and B (#1243) are analyzed alongside ancillary parameters: wind speed (WS), vessel attitude variability (HPRe), cloud coverage, and triplet RMS errors (Ve). Panels (a) and (b) display counts for each threshold and level. Panels (c) and (d) present combined heatmaps comparing parameters, with conditional counts of L0 data in the upper right and the frequency meeting L1 criteria in the lower left.

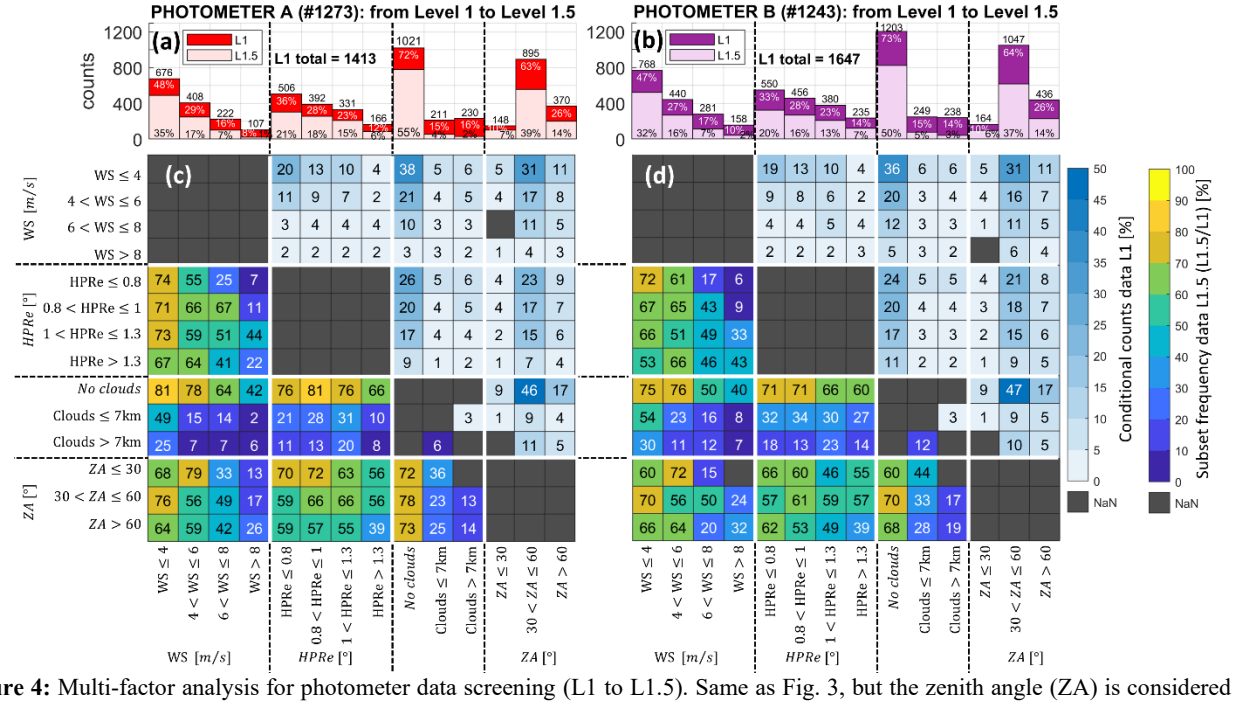

Figure 4: Multi-factor analysis for photometer data screening (L1 to L1.5). Same as Fig. 3, but the zenith angle (ZA) is considered rather than the triplet RMS error.

https://doi.org/10.5194/egusphere-2025-3481
Preprint. Discussion started: 20 August 2025

Figure 4 shows the L1 to L1.5 screening process, highlighting the influence of WS and HPRe. Only 23% of triplet measurements passed L1.5 screening for both photometers, predominantly under low WS (WS<4m/s), stable vessel conditions ($HPRe \leq 1°$), and mid zenith angles (30° < ZA < 60°). Cloud presence is successfully reduced at L1.5. Remaining observations with clouds at high zenith angles likely replicate atmospheric inhomogeneity due to differences between photometer and lidar viewing angles.

Photometer B exhibited better performance under high WS ($> 8\, m/s$) and HPRe (>1.3°), capturing 8% more triplet measurements than photometer A. These differences are attributed to its installation on deck I, equipped with updated tracking software, whereas photometer A, mounted on the mast, was more exposed to wind and vibrations. However, photometer B was subject to occasional obstructions, reducing its L1.5 efficiency across all zenith angles under clear skies.

The L1 performance of both ship-adapted photometer (~40%) was approximately 10% lower than that of land-based AERONET sites in the region. Moreover, Torres et al. (2025) reported strong correlations ($R > 0.96$) between photometers A and B for AOD measurements across various wavelengths, underscoring their reliability under challenging conditions. Comparisons with the AERONET site at Saint-Denis (La Réunion Island) further validated the accuracy of the measurements. Coupled with the multifactor analysis, these findings provide valuable insights to inform and guide further development of the instrument.

3.3 Deriving aerosol properties profiles

The study employs the Klett-Fernald inversion method (Klett, 1981, 1985; Fernald, 1984) to solve the underdetermined lidar equation (Eq. 1). By defining the aerosol extinction-to-backscatter ratio (lidar ratio, LR), the equation is reformulated as a Bernoulli differential equation(Weitkamp, 2005; Speidel and Vogelmann, 2023). The solution depends on boundary conditions defined by the position of an altitude reference zone:

- Backward solution: Reference zone in the far range, dominated by molecular contributions (same as Rayleigh Fit).
- Forward solution: Reference zone near the ground, where aerosol attenuation can be derived or approximated to 1.

In the case of the TRANSAMA campaign, only backward solution is considered, based on daily variations in the range detection limits, as discussed in Sanchez-Barrero et al. (2024). The effective LR (i.e., vertically constant) was iteratively varied to constrain the solution using column-integrated AOD from photometer measurements. As results, vertical profiles of aerosol BSC (β_{aer} in $m^{-1}\ sr^{-1}$) and EXT (α_{aer} in m^{-1}) are derived (Mortier et al., 2013; Popovici et al., 2018). Molecular BSC and EXT profiles were derived from GDAS (Global Data Assimilation System) data or a tropical standard atmosphere model. GDAS meteorological data is publicly available through NOAA Air resources laboratory (https://www.ready.noaa.gov/READYamet.php, last access: May 9 2025).

https://doi.org/10.5194/egusphere-2025-3481
Preprint. Discussion started: 20 August 2025

3.3.1 Uncertainties

Uncertainties are estimated using error propagation from the signal processing by means of first-order derivatives (Russell et al., 1979; Sasano et al., 1985; Kovalev, 1995; Welton and Campbell, 2002; Rocadenbosch et al., 2012; Mortier et al., 2013; Sicard et al., 2020; Sanchez Barrero et al., 2024). Main error sources included overlap function estimation, after-pulse and background noise. Standard deviations from overlap corrections and calibrations were propagated from RCS to aerosol retrievals. LR uncertainty was constrained by matching AOD uncertainties (±0.01) in the iterative solution. Errors in molecular properties are negligible.

4 Results and discussion

Building on the instrumentation and methodologies, this section presents the application of lidar and photometer observations to study aerosol properties variability during the TRANSAMA campaign, offering insights into spatio-temporal variations and aerosol events encountered across the maritime environment. Section 4.1 provides a general overview, the atmospheric structure is discussed in Section 4.2, and selected case studies of transatlantic aerosol transport are analyzed in Section 4.3.

4.1 Aerosol variability during TRANSAMA

The TRANSAMA campaign comprised three segments: the South Indian Ocean (21–28 April), the South Atlantic Ocean (29 April–11 May), and the North Atlantic Ocean (12–15 May).

An overview of synoptic meteorological conditions, vessel trajectory, and local meteorology is presented in Figure 5. Geopotential height maps at 850 hPa (Figs. 5a–c) reveal large-scale atmospheric dynamics, while temporal series include vessel position and motion (Figs. 5d–e) and meteorological conditions (Figs. 5f–h) such as temperature (T), relative humidity (RH), apparent wind speed (AWS) and direction (AWD), as well as true wind speed (TWS) and direction (TWD). Data smoothing (3-hour moving averages) was applied for clarity, with boundaries between campaign segments marked by vertical black lines. Geopotential height maps were generated using NOAA/ESRL reanalysis data through Physical Sciences Laboratory imagery tools (http://psl.noaa.gov/, last access: May 9 2025). Additional meteorological variables, including sea surface temperature and wind vectors, were analyzed but are not showed here for brevity.

Aerosol properties were assessed using a combination of lidar and photometer data. Figure 6 illustrates the spatio-temporal variability in lidar and photometer observations. NRB profiles (Fig. 6a) highlight aerosol and cloud distributions, while photometer observations of AOD at 440 nm (Fig. 6b) and EAE at 440–870 nm (Fig. 6c) provide aerosol size and concentration insights. Both L1 and L1.5 levels of photometer observations are plotted. The campaign encountered “clean” marine conditions with AOD at 440 nm of 0.08 ± 0.04 and EAE at 440–870 nm of 0.5 ± 0.2. Active sensing restrictions in Madagascar, South

https://doi.org/10.5194/egusphere-2025-3481
Preprint. Discussion started: 20 August 2025

Africa, and Brazilian territorial waters limited lidar observations; however, passive photometer measurements continued with exception in Brazil's coastal zones.

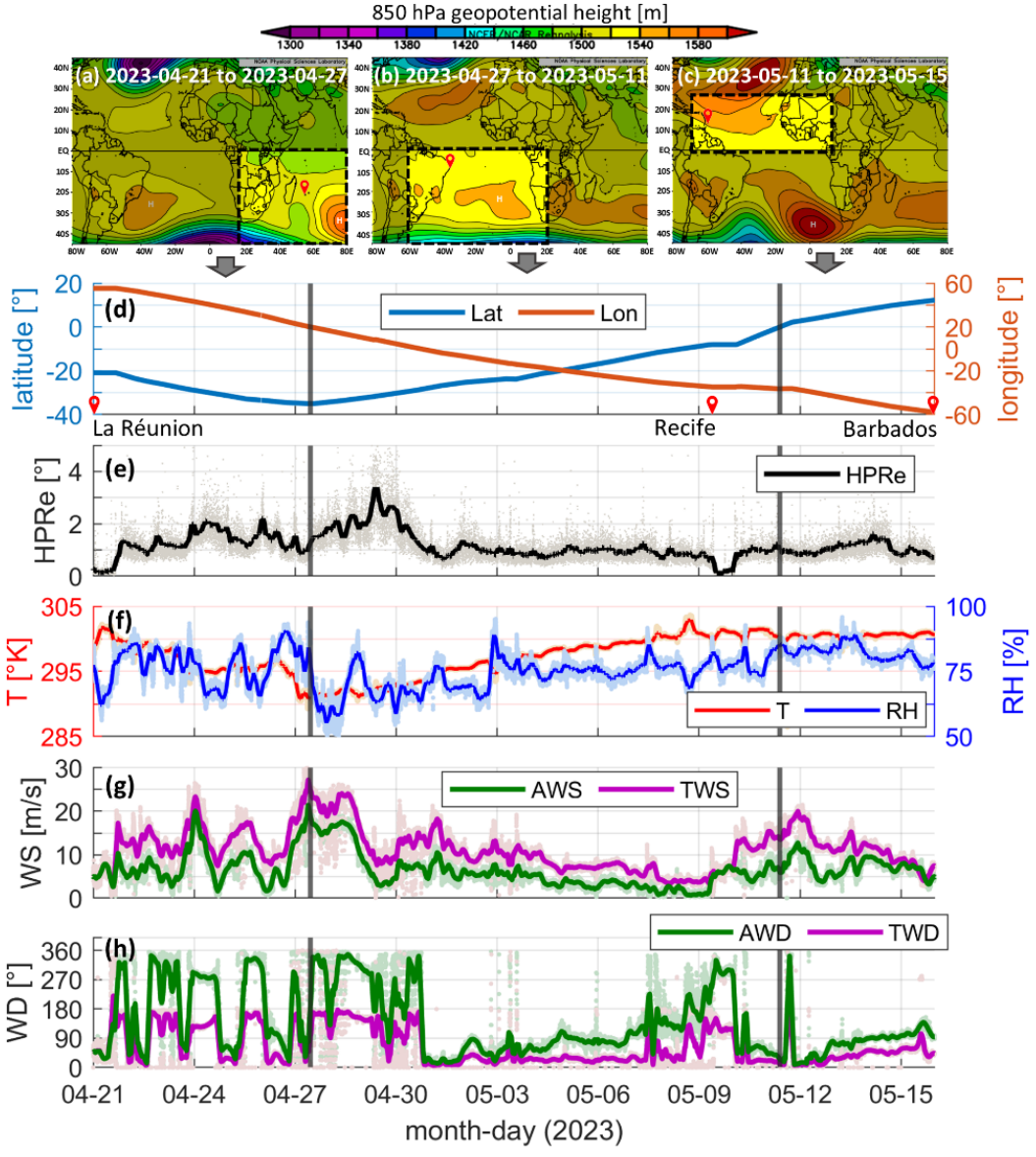

Figure 5: Overview of atmospheric and vessel motion data during the TRANSAMA campaign (April–May 2023). Synoptic meteorological conditions are shown using 850 hPa geopotential height maps for (a) April 21–27, (b) April 27–May 11, and (c) May 11–15. Temporal data for the RV's trajectory are presented in (d) latitude and longitude, (e) the combined RMSE of heading, pitch, and roll (HPRe), (f) temperature (T) and relative humidity (RH), (g) apparent (AWS) and true (TWS) wind speed, and (h) apparent (AWD) and true (TWD) wind direction. Red markers denote ports: La Réunion, Recife, and Barbados. Vertical black lines separate data for the South Indian, South Atlantic, and North Atlantic Oceans. Geopotential height maps were produced using NOAA/ESRL Physical Sciences Laboratory tools (http://psl.noaa.gov/ , last access: May 9 2025).

https://doi.org/10.5194/egusphere-2025-3481
Preprint. Discussion started: 20 August 2025

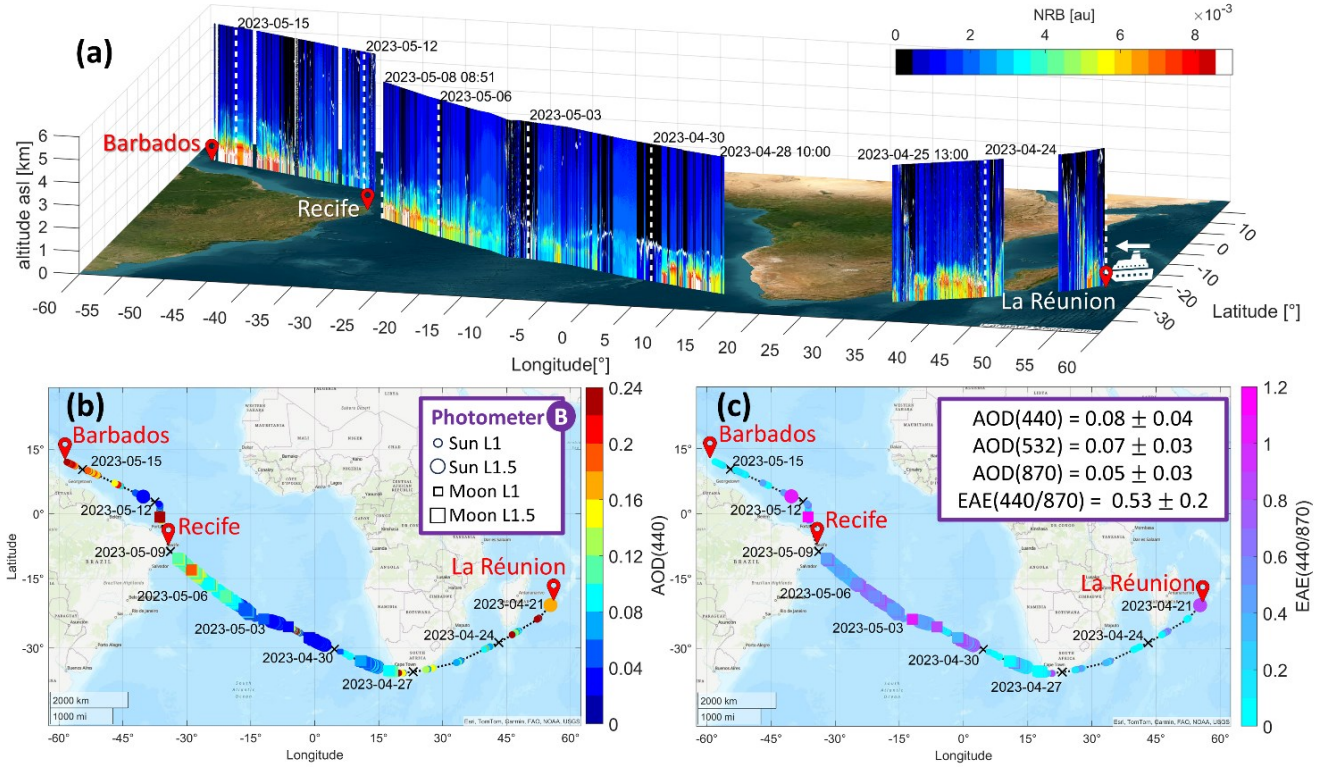

Figure 6: Spatio-temporal variability of aerosol properties during the TRANSAMA campaign (21 April–15 May 2023) aboard the RV *Marion Dufresne II*. Measurements were conducted along the route from La Réunion Island to Barbados. (a) 3D variation of NRB at 532 nm from lidar measurements overlaid on a true-color image of the covered regions. (b) AOD at 440 nm and (c) EAE at 440/870 nm derived from photometer B observations, displayed on topographic maps. Photometer data include L1 and L1.5 solar and lunar observations. Red pins mark the ports at Le Port (La Réunion), Recife (Brazil), and Bridgetown (Barbados).

South Indian Ocean (21-27 April 2023)

The campaign's initial segment over the southwestern Indian Ocean was influenced by the Agulhas Current's retroflection, promoting storm activity and rainfall (Lutjeharms and Van Ballegooyen, 1988). A high-pressure system moving eastward supported the passage of a weak low-pressure system (Ndarana et al., 2023) near Madagascar's southern coast (Fig. 5a). Sea surface declined ~0.5 K per degree latitude (not shown here), with sharp air temperature decrease near South Africa's southern tip (T in Fig. 5f), accompanied by reduced humidity (RH in Fig. 5f) and elevated wind speeds (~20 m/s from the SSE, TWS in Figs. 5g-h). Vessel motion variability increased (HPRe > 1.3° in Fig. 5e), consistent with synoptic conditions (Fig. 5a).

https://doi.org/10.5194/egusphere-2025-3481
Preprint. Discussion started: 20 August 2025

Persistent low clouds (see lidar NRB profiles, Fig. 6a) and rainfall reduced photometer data acquisition (Figs. 6b-c). L1.5 observations were primarily obtained during docking at La Réunion (April 21), where AOD(440) values reached 0.16, and EAE(440–870) indicated presence of fine aerosols, likely linked to urban emissions and volcanic degassing.

South Atlantic Ocean (27 April-11 May 2023)

The second segment traversed the South Atlantic, marked by interactions between the warm Agulhas and cold Benguela currents, fostering arid conditions along Africa's southwest coast (Shannon and Nelson, 1996). Initial conditions (April 27–30) included elevated wind speeds (TWS>20 m/s IN Fig. 5g) and vessel motion (HPRe ~3° in Fig. 5e). Winds eased as high-pressure systems dominated the central South Atlantic (Fig. 5b), producing fair weather under the St. Helena anticyclone (Tyson and Preston-White, 2000). Sea surface temperatures increased (~0.3 K per degree latitude), with TWS < 10 m/s (Fig. 5g) from the north-northeast (Fig. 5e) and HPRe between 0.5–1.3 (Fig. 5e).

Both lidar and photometer were able to measure continuously during this segment, thanks to the favorable conditions. Lidar observations revealed transient clouds (i.e., short lived or short presence) within the first 2 km and thin aerosol layers above the MBL (Fig. 6a). Photometer AOD(440) values ranging 0.03-0.1 (Fig. 6b), with EAE(440/870) ranging 0.4–0.8 (Fig. 6c), yelling 'pristine' marine conditions (Hamilton et al., 2014), and consistent with clean marine aerosol classifications (Kumar et al., 2017; Ranaivombola et al., 2023). Near Brazilian territorial waters, AOD increased to 0.15, and EAE rose to 0.6–0.9, suggesting coastal-urban influences.

North Atlantic Ocean (11-15 May 2023)

The tropical North Atlantic was characterized by stable temperatures (~301 K in Fig. 5f), moderate-to-strong wind speeds (10–18 m/s from the east, TWS in Figs. 5g-h), and moderate HPRe (Fig. 5e). Elevated evaporation rates supported frequent low-level cloud formation, confirmed by lidar observations (Fig. 6a). High-altitude clouds were also detected (see Sect. 4.2), limiting photometer measurements passing to L1.5 (see Sect. 3.2.1). Moreover, the tropical Atlantic Ocean is influenced by the intertropical convergence zone (ITCZ) shifting northwards during the boreal summer and leading the way for Saharan Air Layer (SAL) transport (Prospero and Carlson, 1972; Barreto et al., 2022). An episode of SAL transport was identified through external dust monitoring (Barcelona Dust Regional Center, https://dust.aemet.es/, last access: May 09 2025), but cloud cover (both low level clouds and cirrus) unable detailed lidar-photometer analysis.

This overview lays the foundation for a detailed examination of atmospheric structure, focusing on vertical aerosol distributions and insight into interaction of clouds and aerosols, as discussed in the next section.

https://doi.org/10.5194/egusphere-2025-3481
Preprint. Discussion started: 20 August 2025

4.2 Atmospheric structure

Lidar measurements accounted for 73% of the total navigation time (25 days) from La Réunion to Barbados, generating 26,215 one-minute profiles. Among these, 53 % were flagged as cloud-contaminated. Figure 7a illustrates histograms of cloud and aerosol layer presence across 150 m altitude bins, determined using the gradient method described in Section 3.1.3.

Cloud coverage extended over a broad altitude range, with cirrus clouds reaching above 7 km and up to the tropopause (~17 km near the equator). High-altitude cirrus clouds (>13 km) were observed exclusively within ±5° of the equator, where the tropopause is higher compared to subtropical regions. Cloud occurrence was highest (>10%) below 2 km, coinciding with increased aerosol concentrations. However, cloud presence may be slightly underestimated due to the thresholds applied during automatic detection. Transient clouds in the lower troposphere and high cirrus clouds masked by noise presented challenges for detection, impacting the subsequent inversion.

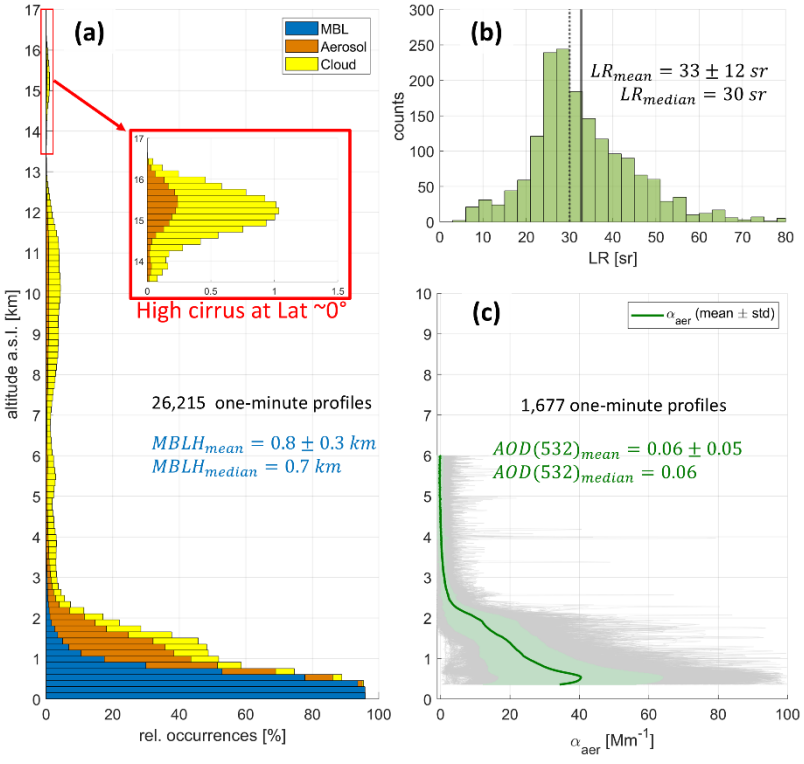

Figure 7: Aerosol vertical distribution derived from lidar and photometer. (a) The occurrence of the MBL, aerosol and cloud layers are presented along with the aerosol (b) effective LR and (c) extinction coefficient profiles.

The mean (median) MBL top height (MBLH), determined for the campaign, was 0.8 ± 0.3 km (0.7 km), showing minimal daytime growth. These findings align with prior studies suggesting MBL heights over remote oceans, coastal regions, and islands typically range between 0.5 km and 1.5 km (Flamant et al., 1997; Bates et al., 2002; Cosma-Averseng et al., 2003; Luo et al., 2014, 2016; Bohlmann et al., 2018; Díaz et al., 2019; Barreto et al., 2022). Unlike the daily evolution observed over

https://doi.org/10.5194/egusphere-2025-3481
Preprint. Discussion started: 20 August 2025

land, the oceanic MBL displayed limited daily growth when the vessel was distant from coastlines, primarily due to the high heat capacity of water (Stull, 1988; Oke, 2009). As noted in Section 4.1, temperatures showed latitudinal increases towards equator rather than daily variations.

Comparatively, Bohlmann et al. (2018) reported lower MBLH (300–500 m) in a two-day case study near Cape Town using multi-wavelength Raman lidar aboard the Polarstern vessel. This discrepancy might reflect the impact of colder waters in the Cape Town region on MBLH growth. Additionally, the lidar system's blind zone (~350 m, Section 3.1.2) limited detailed analysis closer to sea level, underscoring the need of enhanced lidar data acquisition near the surface.

Quality-assured one-minute lidar profiles (Section 3.1.1) underwent an inversion procedure, followed by filtering to exclude profiles with LR exceeding 100 sr or negative extinction coefficients within the first 1.5 km. Campaign data returned 1,677 profiles under clear sky and stable to moderate vessel conditions, mostly over the South Atlantic (Section 4.1). To derive effective LR (Fig. 7b) and extinction profiles (Fig. 7c), stratospheric aerosol contributions from the Hunga underwater volcano eruption (Boichu et al., 2023) were removed. This was done by subtracting the stratospheric AOD from the total column-integrated AOD used to constrain the inversion. By April 2023, Sicard et al. (2025) reported a stabilized aerosol plume at 21ºS between 18.5 and 23.5 km, contributing a stratospheric AOD of 0.012 at 355 nm. Accounting for this contribution (estimated to ~0.01 at 532 nm), the derived mean (median) LR was 33 ± 12 sr (30 sr), with a 27% overestimation (LR = 42±16 sr) when neglecting the stratospheric impact.

While photometer observations identified clean marine aerosols, LR values aligned with studies on contaminated and dried marine aerosols (Duflot et al., 2011; Burton et al., 2013; Floutsi et al., 2023). The mean extinction profile ($10 - 40\ Mm^{-1}$) extended up to 2 km, consistent with low aerosol loadings and aerosol presence above the MBL. Luo et al. (2016) highlighted MBL structure decoupling over the remote Pacific, driven by a weaker temperature inversion capping the MBL, which results in an aerosol layer above it, referred to as the mixing layer. This decoupling influences cloud-top formation as suggested by Luo et al. (2016). Similarly, we observed increased aerosol concentrations above the MBL and higher cloud occurrence.

Having analyzed the atmospheric structure, following section examine the implications of these findings on transatlantic aerosol transport.

4.3 Transatlantic transport

Despite the clean conditions identified in the South Atlantic Ocean, lidar consistently detected persistent thin aerosol plumes above the MBL throughout the route. Under the presence of these layers, profiles exhibited LR values exceeding those typical of pure marine aerosols (Sect. 4.2), suggesting contributions from transported aerosols. Accordingly, a negative correlation

https://doi.org/10.5194/egusphere-2025-3481
Preprint. Discussion started: 20 August 2025

between wind speed and AOD (not shown here) was observed, contrary to previous works demonstrating an increase of marine aerosol production with wind speed (Smirnov et al., 2012; Sun et al., 2024).

Observations during May 4–6, 2023, captured variations in height-time of NRB at 532 nm (Fig. 8a) and time of photometer AOD and EAE (Fig. 8b), benefiting from reduced cloud presence. A noticeable increase in photometer AOD from ~0.04 to ~0.1 was observed after 12:00 UT on May 4, accompanied by EAE(440/870) values ranging between 0.5 and 0.75, indicating mixed aerosol sizes.

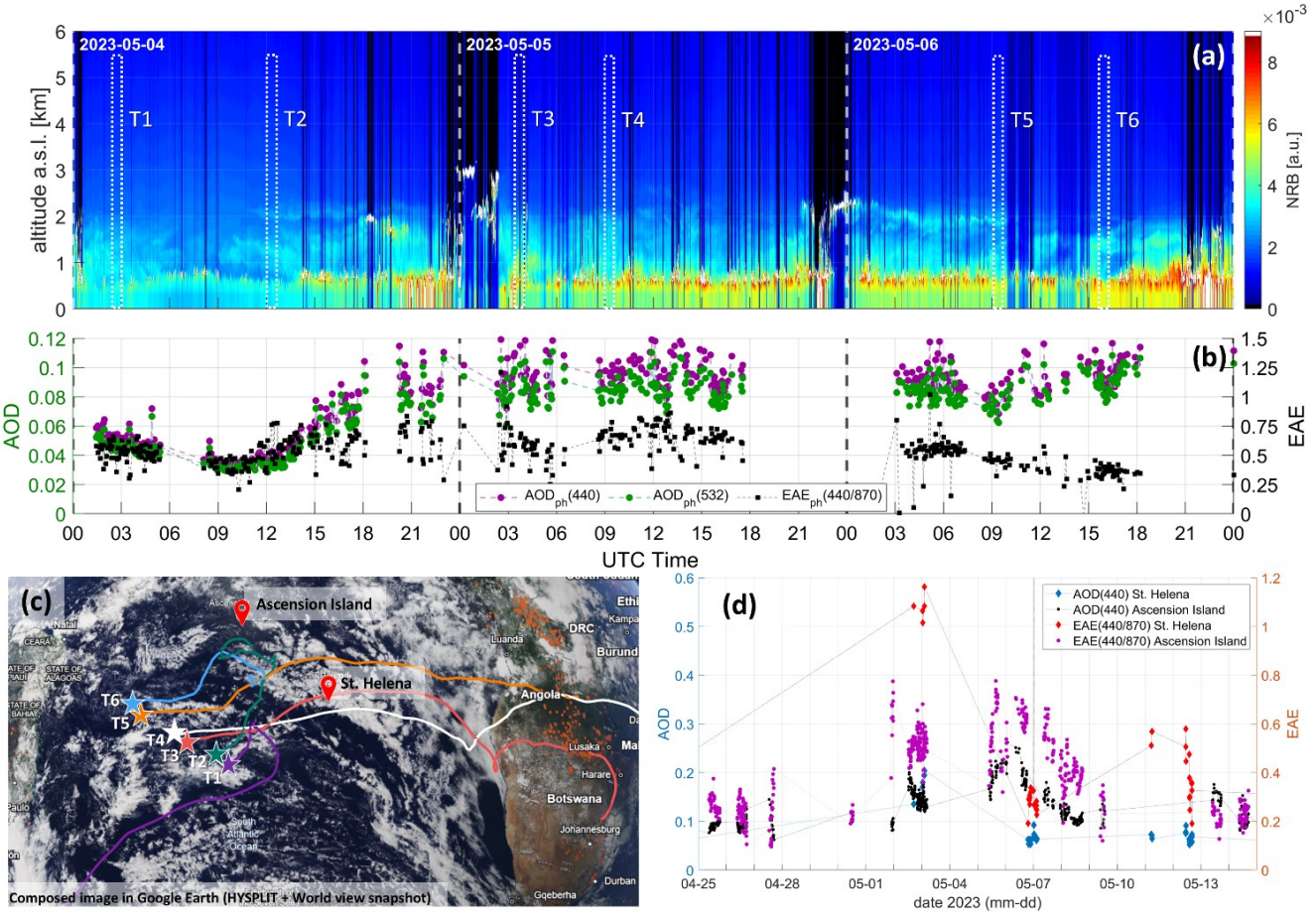

Figure 8: (a) Height-time variations of NRB at 532 nn and (b) temporal sun/moon photometer observations during May 4–6, 2023, are shown. (c) Hysplit back-trajectories for selected time thresholds (T1-T6) plotted on top true color image of MODIS AQUA/TERRA are also presented alongside (d) temporal series of AOD and EAE from two AERONET sites on islands (St. Helena and Ascension Islands). Sunrise and sunset occurred at ~07:00 UT and ~20:00 UT, respectively. The time thresholds considered for the back-trajectories are indicated by dashed white lines in (a). The image in (c) was composed using © Google Earth combining Hysplit and World view outputs in kml format. Photometer data is L1.5 for Marion Dufresne photometer A, sun and moon measurements from AERONET sites are L1.5 and L2 respectively.

https://doi.org/10.5194/egusphere-2025-3481
Preprint. Discussion started: 20 August 2025

To improve lidar SNR, six-time intervals (T1–T6 in dashed white lines on Fig. 8a) were selected for profile averaging (15–30 min). Corresponding back-trajectories were generated using HYSPLIT model (Hybrid Single-Particle Lagrangian Integrated Trajectory; https://www.arl.noaa.gov/hysplit/, last access: May 8 2025), employing GDAS 1-degree resolution meteorological data and tracing aerosol paths up to 2 km altitude over 12 days. These trajectories (Fig. 8c) were overlaid on MODIS AQUA/TERRA true-color imagery, with thermal anomalies marked as orange points (image generated through world view; https://worldview.earthdata.nasa.gov/, last access: May 8 2025). Observations from AERONET sites on St. Helena (elevated, 400 m a.s.l.) and Ascension Islands provided additional context (Fig. 8d). Notably, St. Helena was within the generated back-trajectory paths, while Ascension Island lay outside.

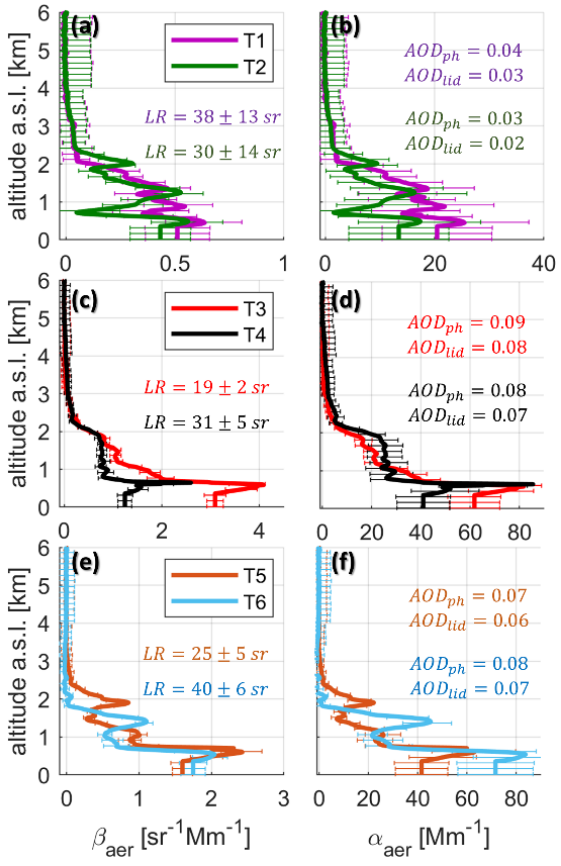

Figure 9: Aerosol properties of averaged profiles during selected time intervals (T1–T6 in Fig. 8a) are shown. Backscatter (a, c, e) and extinction (b, d, f) coefficients profiles are presented. Molecular contributions were estimated using GDAS-1degree meteorological data.

Figure 9 presents the backscatter and extinction coefficient profiles for the selected time intervals, offering insights into aerosol mixing dynamics. Similarly, stratospheric AOD was taken into account for in the inversion (Sect. 4.2). While prior studies (Luo et al., 2016; Sun et al., 2024) linked MBL decoupling to the formation of elevated marine aerosol layers, our observations suggest a more complex mixing process. Aerosol plumes above the MBL, embedded within an extended mixing layer (up to

https://doi.org/10.5194/egusphere-2025-3481
Preprint. Discussion started: 20 August 2025

2 km), exhibited varying contributions from marine and transported aerosols. Extinction and backscatter coefficients were consistently higher within the MBL, indicating dominant AOD contributions from marine sources. For example, aerosol layers in datasets T3 and T5 showed extinction peaks (21 ± 5 Mm^{-1}) less than 50% of MBL values (60 ± 15 Mm^{-1}), with lower LR values ($19 \pm 2\ sr$ and $25 \pm 5\ sr$), closer to typical clean marine conditions. In contrast, other profiles exhibited higher LR values (up to 40 sr), reflecting transported aerosol influence.

Back-trajectories revealed distinct aerosol origins. For datasets T3, T4, and T5 (Fig. 8c), aerosols traveled ~4,500 km over 12 days, originating from wildfire regions in southeastern Angola, southwestern Zambia, and northern Botswana, passing through urban areas. Thermal anomalies identified in these regions (Fig. 8c) suggested fire activity prior the well-known wildfire season in South African region (Ranaivombola et al., 2023 and references therein). Conversely, datasets T1, T2, and T6 suggested air masses circulating over the ocean for ~4 days with potential contributions from the mixed residual biomass-burning-urban emissions. Supporting data from AERONET sites underscored the increase of AOD at 440 nm during the first days of May and the role of fine aerosols. For instance, St. Helena's site (400 m a.s.l.) recorded increased EAE(440/870) above 1 and AOD(440) exceeding 0.1 on May 3, indicative of fine aerosol presence.

While the influence of residual biomass-burning-urban aerosols was modest (extinction peak <30 Mm^{-1}), the persistence of thin aerosol layers throughout the route highlights the significant impact of continental emissions on mid-ocean conditions. These transported aerosols likely contribute to oceanic cloud formation, evidenced by lidar observations of cloud development within the first 2 km in altitude.

5 Conclusions and perspectives

This study highlights the unique insights gained from the TRANSAMA campaign, by using a synergistic combination of micropulse lidar and ship-adapted photometers to investigate aerosol properties in marine environments. The campaign covered the South Indian and Atlantic Oceans, offering the following key findings:

- The vertical profiles derived from lidar data revealed persistent thin aerosol layers above the MBL, even in conditions that might otherwise be misclassified as pristine. These layers predominantly observed over the South Atlantic Ocean, were attributed to long-range transport of residual biomass-burning-urban aerosols from Southern Africa. Back-trajectory analyses and LR values ($33 \pm 12\ sr$) corroborated these findings, aligning with previous studies on contaminated marine aerosols. These results emphasize the significant impact of continental emissions on remote oceanic regions.
- The MBL top height was determined to be 0.8 ± 0.3 km, showing minimal daily evolution, consistent with the thermal inertia of oceanic surfaces. Frequent cloud coverage was observed in lidar profiles, often in association with aerosol presence within and above the MBL. These findings suggest complex aerosol-cloud interactions at low aerosol

https://doi.org/10.5194/egusphere-2025-3481
Preprint. Discussion started: 20 August 2025

loadings, emphasizing the importance of integrated observation networks to unravel aerosol transport mechanisms and their role in cloud formation in pristine regions.

- The coupled micropulse lidar-photometer system demonstrated robust performance in challenging shipborne conditions, effectively capturing vertically resolved aerosol properties despite environmental constraints such as sea spray deposition (for lidar) and sharp vessel motion (for the photometers). This achievement highlights the feasibility of deploying compact, automated remote sensing instruments for continuous aerosol monitoring in marine environments.

Building on these findings, future developments are planned, including the installation of a CIMEL CE376 depolarization lidar aboard the Marion Dufresne in 2025 under the ACTRIS-FR/OBS4CLIM initiative. Additionally, the Data and Service center AERIS will implement a dedicated data processing chain for lidar-photometer mobile observations, contributing to ACTRIS-FR exploratory platforms. The MAP-IO program and ongoing efforts to equip research vessels with advanced Sun-sky-lunar photometers (e.g., Gaia Blu vessel) represent promising steps toward establishing an extended oceanic aerosol monitoring network. The integration of vertically resolved lidar profiles within this network will significantly enhance our understanding of aerosol transport and dynamics, with implications for climate modeling, satellite calibration and validation efforts.

Data availability

Data from photometer land sites are available at AERONET website (https://aeronet.gsfc.nasa.gov, last access: 25 April 2025). The MODIS imagery products are available at NASA Worldview (https://worldview.earthdata.nasa.gov, last access: May 8 2025). HYSPLIT back-trajectories and GDAS-1degree meteorological data were generated using READY (Real-time Environmental Applications and Display sYstem) NOAA ARL website (https://www.ready.noaa.gov, last access: May 8 2025). Marion Dufresne data used in this paper, including meteorological, attitude, lidar and ship-adapted photometer data, are available upon request to the corresponding author.

Authors contributions

MFSB prepared the figures and wrote the manuscript. PG, LB, BT, IEP and MS participated in the discussion of methodology and results. BT, LB, PG and GD lead the ship-adapted photometer developments. TP, LB, IEP and MFSB supported instrumental assessments of lidar. PG, CS, LB, VBR, MS and MFSB contributed to the organization and supported the installation and assessments of instruments aboard the *Marion Dufresne II* RV during TRANSAMA campaign. FD, RDF, TP and LB assured the data transmission to the LOA server and NRT data treatment.

Competing interests

The authors declare no conflict of interest.

https://doi.org/10.5194/egusphere-2025-3481
Preprint. Discussion started: 20 August 2025

Acknowledgements

This work was supported by the ESA-funded project QA4EO (Quality Assurance Framework for Earth Observation), the EUMETSAT-funded project FRM4AER (Fiducial Reference Measurements for Copernicus Aerosol Product Cal/Val Activities), the Horizon Europe European Research Council (project REALISTIC, grant no. 101086690), the Agence Nationale de la Recherche (project OBS4CLIM, grant no. ANR-21-ESRE-0013) and CNES through the projects EECLAT, AOS, and EXTRA-SAT.

MAP-IO was funded by the European Union through the ERDF programme, the University of La Réunion, the SGAR-Réunion, the Région Réunion, the CNRS, IFREMER, and the Flotte Océanographique Française. The technical developments of the shipborne photometer are part of the joint laboratory AGORA-LAB (a collaboration between LOA and CIMEL Electronique).

The authors highly acknowledge the support of TAAF, IFREMER, LDAS, and GENAVIR for their assistance in the installation and maintenance of scientific instruments aboard the Marion Dufresne II RV. Special thanks are also extended to the technical teams of LACy and OSU-R for their efforts in data acquisition and instrument maintenance. The authors also thank the principal investigators (Pawan Gupta and Elena Lind) effort in establishing and maintaining St. Helena and Ascension AERONET sites.

References

Baars, H., Ansmann, A., Engelmann, R., and Althausen, D.: Continuous monitoring of the boundary-layer top with lidar, Atmos. Chem. Phys., 16, 2008.

Barreto, Á., Cuevas, E., Granados-Muñoz, M.-J., Alados-Arboledas, L., Romero, P. M., Gröbner, J., Kouremeti, N., Almansa, A. F., Stone, T., Toledano, C., Román, R., Sorokin, M., Holben, B., Canini, M., and Yela, M.: The new sun-sky-lunar Cimel CE318-T multiband photometer – a comprehensive performance evaluation, Atmos. Meas. Tech., 9, 631–654, https://doi.org/10.5194/amt-9-631-2016, 2016.

Barreto, Á., Cuevas, E., García, R. D., Carrillo, J., Prospero, J. M., Ilić, L., Basart, S., Berjón, A. J., Marrero, C. L., Hernández, Y., Bustos, J. J., Ničković, S., and Yela, M.: Long-term characterisation of the vertical structure of the Saharan Air Layer over the Canary Islands using lidar and radiosonde profiles: implications for radiative and cloud processes over the subtropical Atlantic Ocean, Atmos. Chem. Phys., 22, 739–763, https://doi.org/10.5194/acp-22-739-2022, 2022.

Bates, T. S., Coffman, D. J., Covert, D. S., and Quinn, P. K.: Regional marine boundary layer aerosol size distributions in the Indian, Atlantic, and Pacific Oceans: A comparison of INDOEX measurements with ACE-1, ACE-2, and Aerosols99, J. Geophys. Res., 107, https://doi.org/10.1029/2001JD001174, 2002.

Bechtold, P. and Siebesma, P.: Organization and Representation of Boundary Layer Clouds, J. Atmos. Sci., 55, 888–895, https://doi.org/10.1175/1520-0469(1998)055<0888:OAROBL>2.0.CO;2, 1998.

Bohlmann, S., Baars, H., Radenz, M., Engelmann, R., and Macke, A.: Ship-borne aerosol profiling with lidar over the Atlantic Ocean: from pure marine conditions to complex dust–smoke mixtures, Atmos. Chem. Phys., 18, 9661–9679, https://doi.org/10.5194/acp-18-9661-2018, 2018.

https://doi.org/10.5194/egusphere-2025-3481
Preprint. Discussion started: 20 August 2025

Boichu, M., Grandin, R., Blarel, L., Torres, B., Derimian, Y., Goloub, P., Brogniez, C., Chiapello, I., Dubovik, O., Mathurin, T., Pascal, N., Patou, M., and Riedi, J.: Growth and Global Persistence of Stratospheric Sulfate Aerosols From the 2022 Hunga Tonga–Hunga Ha'apai Volcanic Eruption, JGR Atmospheres, 128, e2023JD039010, https://doi.org/10.1029/2023JD039010, 2023.

Boucher, O., D. Randall, P. Artaxo, C. Bretherton, G. Feingold, P. Forster, V.-M. Kerminen, Y. Kondo, H. Liao, U., and Lohmann, P. Rasch, S.K. Satheesh, S. Sherwood, B. Stevens and X.Y. Zhang: Clouds and Aerosols, in: Climate Change 2013: The Physical Science Basis. Contribution of Working Group I to the Fifth Assessment Report of the Intergovernmental Panel on Climate Change, Cambridge University Press, Cambridge, United Kingdom and New York, NY, USA, 2013.

Brooks, I. M.: Finding Boundary Layer Top: Application of a Wavelet Covariance Transform to Lidar Backscatter Profiles, J. Atmos. Oceanic Technol., 20, 1092–1105, https://doi.org/10.1175/1520-0426(2003)020<1092:FBLTAO>2.0.CO;2, 2003.

Burton, S. P., Ferrare, R. A., Vaughan, M. A., Omar, A. H., Rogers, R. R., Hostetler, C. A., and Hair, J. W.: Aerosol classification from airborne HSRL and comparisons with the CALIPSO vertical feature mask, Aerosols/Remote Sensing/Validation and Intercomparisons, https://doi.org/10.5194/amtd-6-1815-2013, 2013.

Chazette, P. and Totems, J.: Lidar Profiling of Aerosol Vertical Distribution in the Urbanized French Alpine Valley of Annecy and Impact of a Saharan Dust Transport Event, Remote Sensing, 15, 1070, https://doi.org/10.3390/rs15041070, 2023.

Chazette, P., Dabas, A., Sanak, J., Lardier, M., and Royer, P.: French airborne lidar measurements for Eyjafjallajökull ash plume survey, Atmos. Chem. Phys., 12, 7059–7072, https://doi.org/10.5194/acp-12-7059-2012, 2012.

Chazette, P., Flamant, C., Totems, J., Gaetani, M., Smith, G., Baron, A., Landsheere, X., Desboeufs, K., Doussin, J.-F., and Formenti, P.: Evidence of the complexity of aerosol transport in the lower troposphere on the Namibian coast during AEROCLO-sA, Atmos. Chem. Phys., 19, 14979–15005, https://doi.org/10.5194/acp-19-14979-2019, 2019.

Cosma-Averseng, S., Flamant, C., Pelon, J., Palm, S. P., and Schwemmer, G. K.: The cloudy atmospheric boundary layer over the subtropical South Atlantic Ocean: Airborne-spaceborne lidar observations and numerical simulations, J. Geophys. Res., 108, 2002JD002368, https://doi.org/10.1029/2002JD002368, 2003.

Díaz, J. P., Expósito, F. J., Pérez, J. C., González, A., Wang, Y., Haimberger, L., and Wang, J.: Long-Term Trends in Marine Boundary Layer Properties over the Atlantic Ocean, Journal of Climate, 32, 2991–3004, https://doi.org/10.1175/JCLI-D-18-0219.1, 2019.

Dieudonné, E., Chazette, P., Marnas, F., Totems, J., and Shang, X.: Lidar profiling of aerosol optical properties from Paris to Lake Baikal (Siberia), Atmos. Chem. Phys., 15, 5007–5026, https://doi.org/10.5194/acp-15-5007-2015, 2015.

Dubovik, O. and King, M. D.: A flexible inversion algorithm for retrieval of aerosol optical properties from Sun and sky radiance measurements, J. Geophys. Res., 105, 20673–20696, https://doi.org/10.1029/2000JD900282, 2000.

Duflot, V., Royer, P., Chazette, P., Baray, J.-L., Courcoux, Y., and Delmas, R.: Marine and biomass burning aerosols in the southern Indian Ocean: Retrieval of aerosol optical properties from shipborne lidar and Sun photometer measurements, J. Geophys. Res., 116, D18208, https://doi.org/10.1029/2011JD015839, 2011.

Duflot, V., Bègue, N., Pouliquen, M.-L., Goloub, P., and Metzger, J.-M.: Aerosols on the Tropical Island of La Réunion (21°S, 55°E): Assessment of Climatology, Origin of Variability and Trend, Remote Sensing, 14, 4945, https://doi.org/10.3390/rs14194945, 2022.

https://doi.org/10.5194/egusphere-2025-3481
Preprint. Discussion started: 20 August 2025

Eck, T. F., Holben, B. N., Reid, J. S., Arola, A., Ferrare, R. A., Hostetler, C. A., Crumeyrolle, S. N., Berkoff, T. A., Welton, E. J., Lolli, S., Lyapustin, A., Wang, Y., Schafer, J. S., Giles, D. M., Anderson, B. E., Thornhill, K. L., Minnis, P., Pickering, K. E., Loughner, C. P., Smirnov, A., and Sinyuk, A.: Observations of rapid aerosol optical depth enhancements in the vicinity of polluted cumulus clouds, Atmos. Chem. Phys., 14, 11633–11656, https://doi.org/10.5194/acp-14-11633-2014, 2014.

Fernald, F. G.: Analysis of atmospheric lidar observations: some comments, Appl. Opt., 23, 652, https://doi.org/10.1364/AO.23.000652, 1984.

Flamant, C., Pelon, J., Flamant, P. H., and Durand, P.: LIDAR DETERMINATION OF THE ENTRAINMENT ZONE THICKNESS AT THE TOP OF THE UNSTABLE MARINE ATMOSPHERIC BOUNDARY LAYER, Boundary-Layer Meteorology, 83, 247–284, https://doi.org/10.1023/A:1000258318944, 1997.

Floutsi, A. A., Baars, H., Engelmann, R., Althausen, D., Ansmann, A., Bohlmann, S., Heese, B., Hofer, J., Kanitz, T., Haarig, M., Ohneiser, K., Radenz, M., Seifert, P., Skupin, A., Yin, Z., Abdullaev, S. F., Komppula, M., Filioglou, M., Giannakaki, E., Stachlewska, I. S., Janicka, L., Bortoli, D., Marinou, E., Amiridis, V., Gialitaki, A., Mamouri, R.-E., Barja, B., and Wandinger, U.: DeLiAn – a growing collection of depolarization ratio, lidar ratio and Ångström exponent for different aerosol types and mixtures from ground-based lidar observations, Atmos. Meas. Tech., 16, 2353–2379, https://doi.org/10.5194/amt-16-2353-2023, 2023.

Formenti, P., D'Anna, B., Flamant, C., Mallet, M., Piketh, S. J., Schepanski, K., Waquet, F., Auriol, F., Brogniez, G., Burnet, F., Chaboureau, J.-P., Chauvigné, A., Chazette, P., Denjean, C., Desboeufs, K., Doussin, J.-F., Elguindi, N., Feuerstein, S., Gaetani, M., Giorio, C., Klopper, D., Mallet, M. D., Nabat, P., Monod, A., Solmon, F., Namwoonde, A., Chikwililwa, C., Mushi, R., Welton, E. J., and Holben, B.: The Aerosols, Radiation and Clouds in Southern Africa Field Campaign in Namibia: Overview, Illustrative Observations, and Way Forward, Bulletin of the American Meteorological Society, 100, 1277–1298, https://doi.org/10.1175/BAMS-D-17-0278.1, 2019.

Giles, D. M., Sinyuk, A., Sorokin, M. G., Schafer, J. S., Smirnov, A., Slutsker, I., Eck, T. F., Holben, B. N., Lewis, J. R., Campbell, J. R., Welton, E. J., Korkin, S. V., and Lyapustin, A. I.: Advancements in the Aerosol Robotic Network (AERONET) Version 3 database – automated near-real-time quality control algorithm with improved cloud screening for Sun photometer aerosol optical depth (AOD) measurements, Atmos. Meas. Tech., 12, 169–209, https://doi.org/10.5194/amt-12-169-2019, 2019.

Govin A., Chiessi C.M., and cruise participants (2024). Cruise report of AMARYLLIS- AMAGAS II (VT180, MD241), Paramaribo (Suriname) – Recife (Brazil), 12/06/2023- 03/07/2023. 283 pp. https://doi.org/10.13155/98738.

Granados-Muñoz, M. J., Navas-Guzmán, F., Bravo-Aranda, J. A., Guerrero-Rascado, J. L., Lyamani, H., Fernández-Gálvez, J., and Alados-Arboledas, L.: Automatic determination of the planetary boundary layer height using lidar: One-year analysis over southeastern Spain: DETERMINATION OF THE PBL HEIGHT, J. Geophys. Res., 117, n/a-n/a, https://doi.org/10.1029/2012JD017524, 2012.

Hamilton, D. S., Lee, L. A., Pringle, K. J., Reddington, C. L., Spracklen, D. V., and Carslaw, K. S.: Occurrence of pristine aerosol environments on a polluted planet, Proc. Natl. Acad. Sci. U.S.A., 111, 18466–18471, https://doi.org/10.1073/pnas.1415440111, 2014.

Holben, B. N., Eck, T. F., Slutsker, I., Tanré, D., Buis, J. P., Setzer, A., Vermote, E., Reagan, J. A., Kaufman, Y. J., Nakajima, T., Lavenu, F., Jankowiak, I., and Smirnov, A.: AERONET—A Federated Instrument Network and Data Archive for Aerosol Characterization, Remote Sensing of Environment, 66, 1–16, https://doi.org/10.1016/S0034-4257(98)00031-5, 1998.

https://doi.org/10.5194/egusphere-2025-3481
Preprint. Discussion started: 20 August 2025

Holben, B. N., Eck, T. F., Slutsker, I., Smirnov, A., Sinyuk, A., Schafer, J., Giles, D., and Dubovik, O.: Aeronet's Version 2.0 quality assurance criteria, Asia-Pacific Remote Sensing Symposium, Goa, India, 64080Q, https://doi.org/10.1117/12.706524, 2006.

Hu, Q., Goloub, P., Veselovskii, I., Bravo-Aranda, J.-A., Popovici, I. E., Podvin, T., Haeffelin, M., Lopatin, A., Dubovik, O., Pietras, C., Huang, X., Torres, B., and Chen, C.: Long-range-transported Canadian smoke plumes in the lower stratosphere over northern France, Atmos. Chem. Phys., 19, 1173–1193, https://doi.org/10.5194/acp-19-1173-2019, 2019.

Jaeglé, L., Quinn, P. K., Bates, T. S., Alexander, B., and Lin, J.-T.: Global distribution of sea salt aerosols: new constraints from in situ and remote sensing observations, Atmos. Chem. Phys., 11, 3137–3157, https://doi.org/10.5194/acp-11-3137-2011, 2011.

Kanitz, T., Engelmann, R., Heinold, B., Baars, H., Skupin, A., and Ansmann, A.: Tracking the Saharan Air Layer with shipborne lidar across the tropical Atlantic, Geophysical Research Letters, 41, 1044–1050, https://doi.org/10.1002/2013GL058780, 2014.

Karol, Y., Tanré, D., Goloub, P., Vervaerde, C., Balois, J. Y., Blarel, L., Podvin, T., Mortier, A., and Chaikovsky, A.: Airborne sun photometer PLASMA: concept, measurements, comparison of aerosol extinction vertical profile with lidar, Atmos. Meas. Tech., 6, 2383–2389, https://doi.org/10.5194/amt-6-2383-2013, 2013.

Klett, J. D.: Stable analytical inversion solution for processing lidar returns, Appl. Opt., 20, 211, https://doi.org/10.1364/AO.20.000211, 1981.

Klett, J. D.: Lidar inversion with variable backscatter/extinction ratios, Appl. Opt., 24, 1638, https://doi.org/10.1364/AO.24.001638, 1985.

Koren, I., Dagan, G., and Altaratz, O.: From aerosol-limited to invigoration of warm convective clouds, Science, 344, 1143–1146, https://doi.org/10.1126/science.1252595, 2014.

Kotthaus, S., Bravo-Aranda, J. A., Collaud Coen, M., Guerrero-Rascado, J. L., Costa, M. J., Cimini, D., O'Connor, E. J., Hervo, M., Alados-Arboledas, L., Jiménez-Portaz, M., Mona, L., Ruffieux, D., Illingworth, A., and Haeffelin, M.: Atmospheric boundary layer height from ground-based remote sensing: a review of capabilities and limitations, Atmos. Meas. Tech., 16, 433–479, https://doi.org/10.5194/amt-16-433-2023, 2023.

Kovalev, V. A.: Sensitivity of the lidar solution to errors of the aerosol backscatter-to-extinction ratio: influence of a monotonic change in the aerosol extinction coefficient, Appl. Opt., 34, 3457, https://doi.org/10.1364/AO.34.003457, 1995.

Kovalev, V. A. and Eichinger, W. E.: Elastic Lidar: Theory, Practice and Analysis methods, John Wiley & Sons, 2004.

Kumar, K. R., Kang, N., Sivakumar, V., and Griffith, D.: Temporal characteristics of columnar aerosol optical properties and radiative forcing (2011–2015) measured at AERONET's Pretoria_CSIR_DPSS site in South Africa, Atmospheric Environment, 165, 274–289, https://doi.org/10.1016/j.atmosenv.2017.06.048, 2017.

Lopatin, A., Dubovik, O., Chaikovsky, A., Goloub, P., Lapyonok, T., Tanré, D., and Litvinov, P.: Enhancement of aerosol characterization using synergy of lidar and sun-photometer coincident observations: the GARRLiC algorithm, Atmos. Meas. Tech., 6, 2065–2088, https://doi.org/10.5194/amt-6-2065-2013, 2013.

Lopatin, A., Dubovik, O., Stenchikov, G., Welton, E. J., Shevchenko, I., Fuertes, D., Herreras-Giralda, M., Lapyonok, T., and Smirnov, A.: Comparison of diurnal aerosol products retrieved from combinations of micro-pulse lidar and sun photometer

observations over the KAUST observation site, Atmos. Meas. Tech., 17, 4445–4470, https://doi.org/10.5194/amt-17-4445-2024, 2024.

Luo, T., Yuan, R., and Wang, Z.: Lidar-based remote sensing of atmospheric boundary layer height over land and ocean, Atmos. Meas. Tech., 7, 173–182, https://doi.org/10.5194/amt-7-173-2014, 2014.

Luo, T., Wang, Z., Zhang, D., and Chen, B.: Marine boundary layer structure as observed by A-train satellites, Atmos. Chem. Phys., 16, 5891–5903, https://doi.org/10.5194/acp-16-5891-2016, 2016.

Lutjeharms, J. R. E. and Van Ballegooyen, R. C.: The Retroflection of the Agulhas Current, J. Phys. Oceanogr., 18, 1570–1583, https://doi.org/10.1175/1520-0485(1988)018<1570:TROTAC>2.0.CO;2, 1988.

Mallet, P.-É., Pujol, O., Brioude, J., Evan, S., and Jensen, A.: Marine aerosol distribution and variability over the pristine Southern Indian Ocean, Atmospheric Environment, 182, 17–30, https://doi.org/10.1016/j.atmosenv.2018.03.016, 2018.

Mascaut, F., Pujol, O., Verreyken, B., Peroni, R., Metzger, J. M., Blarel, L., Podvin, T., Goloub, P., Sellegri, K., Thornberry, T., Duflot, V., Tulet, P., and Brioude, J.: Aerosol characterization in an oceanic context around Reunion Island (AEROMARINE field campaign), Atmospheric Environment, 268, 118770, https://doi.org/10.1016/j.atmosenv.2021.118770, 2022.

Morille, Y., Haeffelin, M., Drobinski, P., and Pelon, J.: STRAT: An Automated Algorithm to Retrieve the Vertical Structure of the Atmosphere from Single-Channel Lidar Data, Journal of Atmospheric and Oceanic Technology, 24, 761–775, https://doi.org/10.1175/JTECH2008.1, 2007.

Mortier, A.: Tendances et variabilités de l'aérosol atmosphérique à l'aide du couplage Lidar/Photomètre sur les sites de Lille et Dakar, Universite de Lille 1, 2013.

Mortier, A., Goloub, P., Podvin, T., Deroo, C., Chaikovsky, A., Ajtai, N., Blarel, L., Tanre, D., and Derimian, Y.: Detection and characterization of volcanic ash plumes over Lille during the Eyjafjallajökull eruption, Atmos. Chem. Phys., 13, 3705–3720, https://doi.org/10.5194/acp-13-3705-2013, 2013.

Mortier, A., Goloub, P., Derimian, Y., Tanré, D., Podvin, T., Blarel, L., Deroo, C., Marticorena, B., Diallo, A., and Ndiaye, T.: Climatology of aerosol properties and clear-sky shortwave radiative effects using Lidar and Sun photometer observations in the Dakar site, J. Geophys. Res. Atmos., 121, 6489–6510, https://doi.org/10.1002/2015JD024588, 2016.

Ndarana, T., Lekoloane, L. E., Rammopo, T. S., Reason, C. J. C., Bopape, M.-J. M., Chikoore, H., and Engelbrecht, F. A.: Downstream development during ridging South Atlantic Ocean anticyclones, Clim Dyn, 61, 2865–2883, https://doi.org/10.1007/s00382-023-06717-7, 2023.

Oke, T. R.: Boundary layer climates, 2009.

Pelon, J., Mallet, M., Mariscal, A., Goloub, P., Tanré, D., Bou Karam, D., Flamant, C., Haywood, J., Pospichal, B., and Victori, S.: Microlidar observations of biomass burning aerosol over Djougou (Benin) during African Monsoon Multidisciplinary Analysis Special Observation Period 0: Dust and Biomass-Burning Experiment, J. Geophys. Res., 113, D00C18, https://doi.org/10.1029/2008JD009976, 2008.

Pierce, J. R. and Adams, P. J.: Global evaluation of CCN formation by direct emission of sea salt and growth of ultrafine sea salt, J. Geophys. Res., 111, 2005JD006186, https://doi.org/10.1029/2005JD006186, 2006.

https://doi.org/10.5194/egusphere-2025-3481
Preprint. Discussion started: 20 August 2025

Popovici, I. E., Goloub, P., Podvin, T., Blarel, L., Loisil, R., Unga, F., Mortier, A., Deroo, C., Victori, S., Ducos, F., Torres, B., Delegove, C., Choël, M., Pujol-Söhne, N., and Pietras, C.: Description and applications of a mobile system performing on-road aerosol remote sensing and in situ measurements, Atmospheric Measurement Techniques, 11, 4671–4691, https://doi.org/10.5194/amt-11-4671-2018, 2018.

Popovici, I. E., Deng, Z., Goloub, P., Xia, X., Chen, H., Blarel, L., Podvin, T., Hao, Y., Chen, H., Torres, B., Victori, S., and Fan, X.: Mobile On-Road Measurements of Aerosol Optical Properties during MOABAI Campaign in the North China Plain, Atmosphere, 13, 21, https://doi.org/10.3390/atmos13010021, 2022.

Prospero, J. M. and Carlson, T. N.: Vertical and areal distribution of Saharan dust over the western equatorial north Atlantic Ocean, J. Geophys. Res., 77, 5255–5265, https://doi.org/10.1029/JC077i027p05255, 1972.

Ranaivombola, M., Bègue, N., Bencherif, H., Millet, T., Sivakumar, V., Duflot, V., Baron, A., Mbatha, N., Piketh, S., Formenti, P., and Goloub, P.: Aerosol Optical Properties and Types over Southern Africa and Reunion Island Determined from Ground-Based and Satellite Observations over a 13-Year Period (2008–2021), Remote Sensing, 15, 1581, https://doi.org/10.3390/rs15061581, 2023.

Ranaivombola, M., Bègue, N., Vaz Peres, L., Fazel-Rastgar, F., Sivakumar, V., Krysztofiak, G., Berthet, G., Jegou, F., Piketh, S., and Bencherif, H.: Characterization of aerosol optical depth (AOD) anomalies in September and October 2022 over Skukuza in South Africa, Atmos. Chem. Phys., 25, 3519–3540, https://doi.org/10.5194/acp-25-3519-2025, 2025.

Rocadenbosch, F., Frasier, S., Kumar, D., Lange Vega, D., Gregorio, E., and Sicard, M.: Backscatter Error Bounds for the Elastic Lidar Two-Component Inversion Algorithm, IEEE Trans. Geosci. Remote Sensing, 50, 4791–4803, https://doi.org/10.1109/TGRS.2012.2194501, 2012.

Royer, P., Chazette, P., Sartelet, K., Zhang, Q. J., Beekmann, M., and Raut, J.-C.: Comparison of lidar-derived PM10 with regional modeling and ground-based observations in the frame of MEGAPOLI experiment, Atmos. Chem. Phys., 11, 10705–10726, https://doi.org/10.5194/acp-11-10705-2011, 2011.

Russell, P. B., Swissler, T. J., and McCormick, M. P.: Methodology for error analysis and simulation of lidar aerosol measurements, Appl. Opt., 18, 3783, https://doi.org/10.1364/AO.18.003783, 1979.

Sanchez Barrero, M. F., Popovici, I. E., Goloub, P., Victori, S., Hu, Q., Torres, B., Podvin, T., Blarel, L., Dubois, G., Ducos, F., Bourrianne, E., Lapionak, A., Proniewski, L., Holben, B., Giles, D. M., and LaRosa, A.: Enhancing Mobile Aerosol Monitoring with CE376 Dual-Wavelength Depolarization Lidar, https://doi.org/10.5194/amt-17-3121-2024, 2024.

Sasano, Y., Browell, E. V., and Ismail, S.: Error caused by using a constant extinction/backscattering ratio in the lidar solution, Appl. Opt., 24, 3929, https://doi.org/10.1364/AO.24.003929, 1985.

Shang, X., Chazette, P., and Totems, J.: Analysis of a warehouse fire smoke plume over Paris with an N_2 Raman lidar and an optical thickness matching algorithm, Atmos. Meas. Tech., 11, 6525–6538, https://doi.org/10.5194/amt-11-6525-2018, 2018.

Shannon, L. V. and Nelson, G.: The Benguela: Large Scale Features and Processes and System Variability, in: The South Atlantic, Springer Berlin Heidelberg, Berlin, Heidelberg, 163–210, https://doi.org/10.1007/978-3-642-80353-6_9, 1996.

Sicard, M., Rodríguez-Gómez, A., Comerón, A., and Muñoz-Porcar, C.: Calculation of the Overlap Function and Associated Error of an Elastic Lidar or a Ceilometer: Cross-Comparison with a Cooperative Overlap-Corrected System, Sensors, 20, 6312, https://doi.org/10.3390/s20216312, 2020.

Sicard, M., Baron, A., Ranaivombola, M., Gantois, D., Millet, T., Sellitto, P., Bègue, N., Bencherif, H., Payen, G., Marquestaut, N., and Duflot, V.: Radiative impact of the Hunga stratospheric volcanic plume: role of aerosols and water vapor over Réunion Island (21° S, 55° E), Atmos. Chem. Phys., 25, 367–381, https://doi.org/10.5194/acp-25-367-2025, 2025.

Sinyuk, A., Holben, B. N., Eck, T. F., Giles, D. M., Slutsker, I., Korkin, S., Schafer, J. S., Smirnov, A., Sorokin, M., and Lyapustin, A.: The AERONET Version 3 aerosol retrieval algorithm, associated uncertainties and comparisons to Version 2, Atmos. Meas. Tech., 13, 3375–3411, https://doi.org/10.5194/amt-13-3375-2020, 2020.

Smirnov, A., Holben, B. N., Eck, T. F., Dubovik, O., and Slutsker, I.: Cloud-Screening and Quality Control Algorithms for the AERONET Database, Remote Sensing of Environment, 73, 337–349, https://doi.org/10.1016/S0034-4257(00)00109-7, 2000.

Smirnov, A., Holben, B. N., Slutsker, I., Giles, D. M., McClain, C. R., Eck, T. F., Sakerin, S. M., Macke, A., Croot, P., Zibordi, G., Quinn, P. K., Sciare, J., Kinne, S., Harvey, M., Smyth, T. J., Piketh, S., Zielinski, T., Proshutinsky, A., Goes, J. I., Nelson, N. B., Larouche, P., Radionov, V. F., Goloub, P., Krishna Moorthy, K., Matarrese, R., Robertson, E. J., and Jourdin, F.: Maritime Aerosol Network as a component of Aerosol Robotic Network, J. Geophys. Res., 114, D06204, https://doi.org/10.1029/2008JD011257, 2009.

Smirnov, A., Sayer, A. M., Holben, B. N., Hsu, N. C., Sakerin, S. M., Macke, A., Nelson, N. B., Courcoux, Y., Smyth, T. J., Croot, P., Quinn, P. K., Sciare, J., Gulev, S. K., Piketh, S., Losno, R., Kinne, S., and Radionov, V. F.: Effect of wind speed on aerosol optical depth over remote oceans, based on data from the Maritime Aerosol Network, Atmos. Meas. Tech., 5, 377–388, https://doi.org/10.5194/amt-5-377-2012, 2012.

Speidel, J. and Vogelmann, H.: Correct(ed) Klett–Fernald algorithm for elastic aerosol backscatter retrievals: a sensitivity analysis, Appl. Opt., 62, 861, https://doi.org/10.1364/AO.465944, 2023.

Stull, R.: An introduction to Boundary Layer Meteorology, Kluwer Academic Publishers, 1988.

Sun, K., Dai, G., Wu, S., Reitebuch, O., Baars, H., Liu, J., and Zhang, S.: Effect of wind speed on marine aerosol optical properties over remote oceans with use of spaceborne lidar observations, Atmos. Chem. Phys., 24, 4389–4409, https://doi.org/10.5194/acp-24-4389-2024, 2024.

Szopa, S., V. Naik, B. Adhikary, P. Artaxo, T. Berntsen, W.D. Collins, S. Fuzzi, L. Gallardo, A. Kiendler-Scharr, Z. Klimont, H. Liao, N. Unger, and P. Zanis: Short-lived Climate Forcers, in: Climate Change 2021 – The Physical Science Basis: Working Group I Contribution to the Sixth Assessment Report of the Intergovernmental Panel on Climate Change, Cambridge University Press, https://doi.org/10.1017/9781009157896, 2021.

Torres, B., Blarel, L., Goloub, P., Dubois, G., Sanchez-Barrero, M. F., Popovici, I. E., Maupin, F., Lind, E., Smirnov, A., Slutsker, I., Chimot, J., Gonzalez, R., Sicard, M., Metzger, J. M., and Tulet, P.: Adaptation of the CIMEL-318T to Shipborne Use: Three Years of Automated AERONET-Compatible Aerosol Measurements Onboard the Research Vessel Marion Dufresne, https://doi.org/10.5194/egusphere-2025-1356, 31 March 2025.

Tulet, P., Van Baelen, J., Bosser, P., Brioude, J., Colomb, A., Goloub, P., Pazmino, A., Portafaix, T., Ramonet, M., Sellegri, K., Thyssen, M., Gest, L., Marquestaut, N., Mékiès, D., Metzger, J.-M., Athier, G., Blarel, L., Delmotte, M., Desprairies, G., Dournaux, M., Dubois, G., Duflot, V., Lamy, K., Gardes, L., Guillemot, J.-F., Gros, V., Kolasinski, J., Lopez, M., Magand, O., Noury, E., Nunes-Pinharanda, M., Payen, G., Pianezze, J., Picard, D., Picard, O., Prunier, S., Rigaud-Louise, F., Sicard, M., and Torres, B.: MAP-IO: an atmospheric and marine observatory program on board *Marion Dufresne* over the Southern Ocean, Earth Syst. Sci. Data, 16, 3821–3849, https://doi.org/10.5194/essd-16-3821-2024, 2024.

https://doi.org/10.5194/egusphere-2025-3481
Preprint. Discussion started: 20 August 2025

Tyson, P. D. and Preston-White, R. A.: The weather and climate of southern Africa, Oxford University Press, available at: https://global.oup.com/academic/product/ the-weather-and-climate-of-southern-africa-9780195718065? lang=en&cc=in (last access: 29 April 2019), 2000.

Warneke, C., Schwarz, J. P., Dibb, J., Kalashnikova, O., Frost, G., Al-Saad, J., Brown, S. S., Brewer, Wm. A., Soja, A., Seidel, F. C., Washenfelder, R. A., Wiggins, E. B., Moore, R. H., Anderson, B. E., Jordan, C., Yacovitch, T. I., Herndon, S. C., Liu, S., Kuwayama, T., Jaffe, D., Johnston, N., Selimovic, V., Yokelson, R., Giles, D. M., Holben, B. N., Goloub, P., Popovici, I., Trainer, M., Kumar, A., Pierce, R. B., Fahey, D., Roberts, J., Gargulinski, E. M., Peterson, D. A., Ye, X., Thapa, L. H., Saide, P. E., Fite, C. H., Holmes, C. D., Wang, S., Coggon, M. M., Decker, Z. C. J., Stockwell, C. E., Xu, L., Gkatzelis, G., Aikin, K., Lefer, B., Kaspari, J., Griffin, D., Zeng, L., Weber, R., Hastings, M., Chai, J., Wolfe, G. M., Hanisco, T. F., Liao, J., Campuzano Jost, P., Guo, H., Jimenez, J. L., Crawford, J., and The FIREX-AQ Science Team: Fire Influence on Regional to Global Environments and Air Quality (FIREX-AQ), JGR Atmospheres, 128, https://doi.org/10.1029/2022JD037758, 2023.

Weitkamp, C. (Ed.): Lidar: range-resolved optical remote sensing of the atmosphere, Springer, New York, 455 pp., 2005.

Welton, E. J. and Campbell, J. R.: Micropulse Lidar Signals: Uncertainty Analysis, J. Atmos. Oceanic Technol., 19, 2089–2094, https://doi.org/10.1175/1520-0426(2002)019<2089:MLSUA>2.0.CO;2, 2002.

Yin, Z., Ansmann, A., Baars, H., Seifert, P., Engelmann, R., Radenz, M., Jimenez, C., Herzog, A., Ohneiser, K., Hanbuch, K., Blarel, L., Goloub, P., Dubois, G., Victori, S., and Maupin, F.: Aerosol measurements with a shipborne Sun–sky–lunar photometer and collocated multiwavelength Raman polarization lidar over the Atlantic Ocean, Atmos. Meas. Tech., 12, 5685–5698, https://doi.org/10.5194/amt-12-5685-2019, 2019.